1994

Energy Dependence of Photoion Rotational Distributions.

Heung-cheun Choi
Louisiana State University and Agricultural & Mechanical College

Order Number 9502103

Energy dependence of photoion rotational distributions

Choi, Heung-Cheun, Ph.D.

The Louisiana State University and Agricultural and Mechanical Col., 1994

U·M·I

300 N. Zeeb Rd.
Ann Arbor, MI 48106

ENERGY DEPENDENCE OF PHOTOION ROTATIONAL DISTRIBUTIONS

A Dissertation

Submitted to the Graduate Faculty of the
Louisiana State University and
Agricultural and Mechanical College
in partial fulfillment of the
requirements for the degree of
Doctor of Philosophy

in

The Department of Physics and Astronomy

by
Heung–Cheun Choi
B.Sc., Korea University, 1982
M.S., Korea University, 1984
May 1994

dedicated specially to

my mother

who loved me so much

and to my father and parents in law

who give me so much

and to

my wife

who loves me and takes care of two children

ACKNOWLEDGMENTS

First of all, I wish to express with the most sincere gratitude to my adviser, Professor Poliakoff for his tireless support and encouragement. Without his guidance, this work could not have been completed. It is also my pleasure to acknowledge the people who have been worked with me during the last several years. It has been a good time to discuss with Dr. Sandeep Kakar from personal to scientific topics. I appreciate Dr. Art G. Mihill for helping specially optical alignments, and Raj Rao and Romith Das for helping with this experiment.

I deeply thank Professor Rau and chairman Professor Draayer for visiting me while I was hospitalized during my first year, and my committee members Professors Callaway, Stockbauer and CAMD director Dr. Saile.

Also, I am indebted to K. Wang and V. McKoy for theoretical calculations for this work, and the efforts of the CAMD staff are appreciated.

To my parents and parents-in-law, I couldn't find any way to repay for their endless faith and support, especially, to my mother who didn't say anything about her pains. I would like to give special thanks to my wife for

taking care of two children and always encouraging me. Without her helps, it would be impossible to accomplish my desire. Her faith is truly inestimable.

TABLE OF CONTENTS

ABSTRACT

Highly resolved molecular photoionization is a topic of intense current interest due to insights it provides into fundamental scattering processes. Rotationally resolved data provide a window on the angular momentum composition of the photoelectron and the partitioning of angular momentum between the ion and photoelectron. Since the earliest rotational measurements via photoelectron spectroscopy (PES) of H_2 using resonance lamp excitation, studies have accelerated as a result of experimental innovations. However, all of these recent developments have been limited to threshold or near-threshold ionization phenomena. In order to bypass this constraint, we have employed dispersed fluorescence measurements. This strategy allows us to exploit the broad tunability of synchrotron radiation because the detection bandwidth is uncoupled from the excitation bandwidth. The isoelectronic target molecules N_2 and CO are rotationally cooled by a supersonic expansion, and ionized by synchrotron radiation from a 6-m Plane Grating Monochromator (PGM), at the Louisiana State University Center for Advanced Microstructures and Devices (CAMD). The rotational fluorescence spectra are obtained over the energy range from $20 \leq h\nu_{exc} \leq 220$ eV for N_2 $2\sigma_u^{-1}$ photoionization and from $23 \leq h\nu_{exc} \leq 145$ eV for CO $4\sigma^{-1}$ photoionization. The results of $N_2^+(B^2\Sigma_u^+)$ and $CO^+(B^2\Sigma^+)$ rotational distributions show strikingly different energy dependences. Detailed calculations reveal that the dramatically changing $N_2^+(B^2\Sigma_u^+)$ rotational distributions arise from Cooper minima of *g*- and *d*-waves in the $k\sigma_g$ photoelectron continuum, while the flatness of $CO^+(B^2\Sigma^+)$ rotational distributions results from a delicate balance

between the $4\sigma \rightarrow k\sigma$ *f*-wave shape resonance and the broad *f*-wave enhancement in $k\pi$ photoelectron continuum. Cooper minima for N_2 $2\sigma_u^{-1}$ ionization lead to small ΔN transitions at lower energies and large ΔN transitions at higher energies, while the CO $4\sigma \rightarrow k\sigma$ shape resonance results in larger ΔN transitions over the whole energy range studied. The present studies of $N_2^+(B^2\Sigma_u^+)$ and $CO^+(B^2\Sigma^+)$ rotational distributions illustrate effects of Cooper minima, shape resonances, and *l* mixing in photoelectron continua at energies well beyond the reach of conventional photoelectron spectroscopy. Moreover, these results also demonstrate that rotationally resolved fluorescence is suitable for studies of molecular photoionization dynamics over a broad spectral range.

CHAPTER I.

INTRODUCTION

As a result of the rapid growth of synchrotron radiation facilities, vacuum ultraviolet (VUV) photoionization spectroscopies play a central role in studies of fundamental scattering dynamics. The ability to tune the incident photon energy continuously allows us to vary the scattering energy, thus we can select spectral features of interest with tremendous flexibility. Moreover, we have the experimental ability to investigate how individual rovibronic levels of the ion are influenced by the ionization dynamics. Since photoionization is a half–scattering process in which a collision complex is created by dipole excitation [1–4], it is possible to manipulate the scattering parameters precisely. Thus, photoionization is a rich source of information on fundamental scattering processes, in general. For molecular systems in particular, the escaping electron traverses the anisotropic molecular field, hence it carries the dynamical information on the aspects of the molecular behavior (e.g., vibration [1,2,5–7], rotation [8–18], and alignment [19–21]). Rotationally resolved photoionization is a topic of current interest [9–18,22–26] and plays an important role in studying fundamental intramolecular interactions. Rotationally resolved data provide information on the transfer of angular momentum from the incident photon to the target molecule, the subsequent partitioning of angular momentum between the photoelectron and

the ion core, and the angular momentum composition of the continuum photoelectron [11–17,22–28]. In this study, I exploit detection of dispersed fluorescence from photoions to obtain rotationally resolved results for diatomic photoionization. Most importantly, I will demonstrate that this method allows measurements over a broad spectral range, enabling us to more fully characterize the photoelectron scattering dynamics.

Since the earliest rotationally resolved measurements via photoelectron spectroscopy (PES) of H_2 by Åsbrink using resonant lamp excitation in 1970 [9], there has been increasing interest as a result of experimental innovations with both lasers and photoelectron spectroscopy. In recent years, the combination of resonantly enhanced multiphoton ionization (REMPI) and photoelectron spectroscopy has been useful in illustrating the characteristics of the intermediate electronic state and the dynamics of the excited state photoionization [12,22–24]. The REMPI–PES technique has been successful in photoionization studies for several diatomic molecules, e.g., H_2 [36], D_2 [8], NO [12,22], N_2 [14] and O_2 [11]. Also, the technique of laser–induced fluorescence following REMPI has been further employed for the direct observation of nascent rotational distributions for HBr [26], and N_2 [25], and CO [25]. Recently, molecular photoionization studies using zero-kinetic-energy pulsed-field-ionization (ZEKE–PFI) spectroscopy have been pioneered by Müller–Dethlefs [14] and White [11,17]. Even though these studies have

been powerful tools to understand the fundamental molecular ionization dynamics, rotationally resolved data have been limited to threshold or near-threshold for two reasons. First, the electron energy resolution is limited at high kinetic energies [29]. Second, soft x-ray lasers are not currently available. To put the experimental requirements into perspective, it is useful to examine a typical diatomic sample. With rotational energy spacings on the order of 4 cm^{-1} for diatomic systems, rotationally resolved electron spectra at the photon energy of 220 eV require a resolving power ($E/\Delta E$) of 10^6. That is orders of magnitude beyond the highest resolution photoelectron spectroscopy at corresponding energies [29–31]. While laser techniques provide the opportunity for high resolution work over limited spectral ranges, the synchrotron radiation source is tunable but does not provide high resolving power. The dispersed fluorescence measurement exploits the advantage of the broad tunability of synchrotron radiation. Most importantly, however, the detection bandwidth in the fluorescence measurements is decoupled from (and therefore, not limited by) the excitation bandwidth [6,32]. In order to simplify the analysis of the resulting data, it is necessary to limit the number of rotational target states undergoing photoionization, so the sample molecules are rotationally cooled by a free–jet supersonic molecular beam. Thus, by exploiting advantages demonstrated in earlier fluorescence studies [6,27,28,33], the rotationally resolved fluorescence measurements

provide useful fingerprints of the partitioning of the angular momentum between the photoelectron and photoion over an extended spectral range.

Photoelectron ejection can be considered as a two–step process. First, a photon is absorbed by a bound electron, and angular momentum is transferred to the photoelectron. Secondly, the electron escapes from the ion–photoelectron complex. During the escape of the photoelectron, angular momentum can be exchanged between photoelectron and ion core [3,4,20]. In the anisotropic fields of molecular systems, the angular momentum transfer can be viewed as arising from torques exerted on the outgoing electron, while it can be neglected in the central fields of atomic system [3–4,17,20]. For the single–photon ($J_p = 1$) ionization of the diatomic molecular AB (J_0) to yield $AB^+(J^+) + e^-(l + ½)$, parity selection rules constrain the allowed values for $\Delta J = J^+ - J_0$ to be $\Delta J = l + 3/2,\ l + 1/2,\ \ldots,\ -(l + 1/2),\ -(l + 3/2)$ by the conservation of angular momentum [13,17]. The angular momentum composition l of the photoelectron can lead to a change of total angular momentum ΔJ or alternatively stated, a change of rotational angular momentum $\Delta N = N^+ - N_0$, excluding electron spin in the case that the electron spin is very weakly coupled to internuclear axis [31]. The actual ΔN values that occur over a broad range of electron energies depend sensitively on microscopic aspects of the scattering dynamics. These rotational angular momentum changes ΔN as a function of excitation energies can explain the

dynamical behavior of the photoion rotational distributions that are obtained from the intensities of the fluorescence spectra [31]. To gain insight into the dynamical behavior of the photoion rotational distributions due to the energy dependence of angular momentum changes ΔN, it is necessary to examine the dipole matrix element $\langle f \left| \mu \right| i \rangle$ for the photoejection of an electron from a bound molecular orbital into a continuum orbital [3,17]. In the evaluation of the dipole matrix element, the angular part of the integration proceeds analytically and yields the selection rule on the orbital quantum number between the final and initial photoelectron states. Meanwhile, the radial integral needs to be numerically evaluated by transforming the photoelectron state from a laboratory frame to a rotating molecular frame, and its geometrical analysis can be explained in terms of the angular momentum transfer between ion and photoelectron [3].

Recently, Wang and McKoy calculated partial wave photoelectron matrix elements for the diatomic molecule NO at low photoelectron energies [16,17]. Their calculations demonstrate that the dipole matrix element reveals a central feature unique to molecular photoionization. Whereas only $l = l'$ terms are allowed in the partial wave photoelectron matrix elements for the central fields of the atomic systems, off-diagonal contributions ($l \neq l'$) to photoelectron matrix elements arise in nonspherical fields of the molecular system [17]. In the molecular case, the escaping electron traverses the

anisotropic molecular field and influences the rotation and vibration of the ion [1–4,17,20]. Hence the outgoing electron which experiences anisotropic interactions results in angular momentum coupling between off–diagonal terms of dipole matrix elements and the admixture of angular momentum components. The partitioning of angular momentum between photoelectron and ion is reflected in the partial wave composition of the photoelectron which can be probed by monitoring the angular momentum distribution for the photoions.

Using the calculated dipole matrix elements as an aid, rotationally resolved measurements provide clues for understanding fundamental aspects of molecular photoionization, including effects of Cooper minima and shape resonances. In our study of the photoion rotational fluorescence measurements for the isoelectronic systems N_2 and CO, the results show strikingly unusual and different energy dependences. The presence of Cooper minima (l = 2 and 4) in the photoelectron continuum for the $2\sigma_u^{-1}$ photoionization in N_2 results in strongly energy–dependent photoion rotational distributions, which are observed in experiment. For CO photoionization, an f-wave shape resonance in the $4\sigma \rightarrow k\sigma$ channel leads to the flatness of the rotational distribution over a broad spectral range [31,35]. From results of experimental measurements and theoretical calculations, it is revealed that the angular momentum transfer effects on the rotationally

resolved photoionization and the changes of rotational angular momentum $\Delta N = N^+ - N_0$ can provide valuable propensity rules in molecular photoionization [16,17,34]. There are two central goals of the present study. First, I wish to elucidate the photoionization dynamics using rotationally resolved data which contain information on the angular momentum composition of the photoelectron and on the partitioning of angular momentum between photoelectron and ion core. Secondly, I wish to demonstrate that dispersed fluorescence measurements coupled with rotationally cooled supersonic expansions provide a useful basis for acquiring data over a broad spectral range, enabling synchrotron based investigations to more fully characterize molecular ionization dynamics.

I present the study of the rotational dispersed fluorescence photoionization for the photoejection from the $2\sigma_u^{-1}$ channel of N_2 over the energy range 20 eV $\leq h\nu_{exc} \leq$ 220 eV and for the photoejection from the $4\sigma^{-1}$ channel of CO over 23 eV $\leq h\nu_{exc} \leq$ 145 eV, using synchrotron radiation from the CAMD 6–m plane grating monochromator (PGM). The theoretical and experimental background for this study is reviewed in Ch. II. Chapter III gives the detailed experimental description, including a description of the PGM beam line. In Chapter IV, I discuss the photoion rotational distributions obtained from the dispersed fluorescence measurement and compare our results with the calculations of Wang and McKoy [35].

Finally, the conclusions of this study and future developments are presented in Chapter V.

CHAPTER II.

BACKGROUND

Photoelectron ejection can be considered as a two–step process, i.e., as a first step, absorption of a photon by a bound-state electron occurs with the transfer of angular momentum to the photoelectron, and secondly, the photoelectron escapes from the ion-electron complex [3,4]. During the escape of the photoelectron, angular momentum can be further transferred between the photoelectron and the ion core. For anisotropic fields present in molecular systems, the angular momentum transfer can be viewed as arising from torques exerted on the outgoing electron. By way of contrast, it can be neglected in the central field approximation, where the angular momentum of the photoelectron is conserved [3,4,17], and this molecular "rescattering" is absent. The nature of the angular momentum rescattering in molecular photoionization may be quite complex [3]. To introduce the ideas, I review the theoretical and experimental background. In the theoretical background, the photoionization process is described in terms of relevant dipole matrix elements where the photoelectron state is described by switching from the laboratory frame to a rotating molecular frame [3]. Aspects relevant to the photoion rotational distributions are outlined as follows. First, the geometrical analysis is cast in terms of angular momentum transfer between ion and photoelectron. Second, I describe reasons for changes in the behavior

of the dipole matrix element in terms of the underlying dynamics, and how these are reflected in the photoion angular momentum distributions. In the experimental background, I highlight the advantages and limitations of dispersed fluorescence for studies of rotationally resolved photoionization and also estimate the photoion rotational distribution obtained from the fluorescence spectra for data analysis.

2.1 Theoretical Background

2.1.1 Angular Momentum Transfer

In molecular photoionization, anisotropic fields influence the angular momentum transfer between photoelectron and ion core during the escape of the electron [1–5,17]. The studies of rotationally resolved photoionization can provide information on the interaction of the photoelectron with the ion core, especially on the angular momentum quantum number of the electron emerging from the collision with the photon [1–5,17]. The photoelectron ejection for the molecular photoionization of a diatomic target AB can be described schematically as [4,20] :

$$AB(J_0, \pi_0) + h\nu(J_p = 1, \pi_p = -1) \rightarrow AB^+ (J^+, \pi^+) + e^- (J_e = l + \frac{1}{2}, \pi_e = (-1)^l), \tag{2.1}$$

where the "J"s and "π"s are angular momenta and parities, respectively. In the molecular photoionization, the angular momentum components (l) of the photoelectron may be restricted by the conservation of angular momentum (J) and parity (π) in Eq.(2.2) [3,4,20].

$$\mathbf{J} = \mathbf{J}_0 + \mathbf{J}_p = \mathbf{J}^+ + \mathbf{J}_e$$

$$\pi = (-1)^{J_0+1} = \pm(-1)^{l+J^+}. \qquad (2.2)$$

Parity conservation in the initial and the final states of the system requires a plus or minus sign depending on whether the total wavefunction remains unchanged or changes sign with respect to reflection at the origin [37]. For example, a plus sign is assigned when the ion is Σ^+ and a minus sign is appropriate for a Σ^- state. For single photon ionization, the conservation of angular momentum restricts the changes in total angular momentum ΔJ (excluding nuclear spin) to [13]

$$\Delta J = J^+ - J_0 = (l + 3/2), (l + 1/2), \ldots, -(l + 3/2). \qquad (2.3)$$

The allowed values of ΔJ can be expressed in terms of rotational quantum number N by excluding the electron spin [31,35],

$$\Delta N = N^+ - N_0 = (l + 1), l, \ldots, -(l + 1). \qquad (2.4)$$

An alternative combination of the angular momenta, J_t, can be defined as the angular momentum transferred from the observed to the unobserved reactants [3,4,20],

$$\mathbf{J}_t = \mathbf{J}_p - \mathbf{l} = \mathbf{J}^+ + \mathbf{s} - \mathbf{J}_0 . \qquad (2.5)$$

Since the photon in the electric dipole approximation couples only to the angular momentum of the photoelectron, only the orbital part of $J_e = l + ½$ is replaced in defining the angular momentum transfer J_t. Thus, a particular value of l for the photoelectron results in values of $J_t = |1 - l|$ by focusing only on the incident photon and the photoelectron. In other words, the value of l is restricted to the values J_t and $J_t \pm 1$ [3].

For the N_2 $(X^1\Sigma_g^+) \rightarrow N_2^+$ $(B^2\Sigma_u^+)$ photoionization of N_2, the electronic inversion symmetry ($g \leftrightarrow u$) requires the angular momentum l of the photoelectron to be even from Eq.(2.2), and the values of J_t to be odd [13,38]. Note that the labels gerade (g) or ungerade (u) in the homonuclear molecular are classified depending on whether the electronic wave function is unchanged or changes sign upon the inversion of the electronic coordinates [37]. Therefore, the allowed values of ΔN for the $^1\Sigma_g^+ \rightarrow {}^2\Sigma_u^+$ photoionization of N_2 can be extracted from Eq.(2.4) as $\Delta N = \pm(l + 1), \pm(l - 1), \ldots$ for only even angular momentum l [13,38]. Thus, the ejected photoelectron carrying angular momentum l experiences anisotropic

interactions in the molecular fields, leading to $l = 0, 2, 4, \ldots$ or $\Delta N = \pm 1, \pm 3, \pm 5, \ldots$. The actual ΔN values that occur depend sensitively on the scattering dynamics [31]. The key point is that the energy dependence of the angular momentum changes provides a powerful tool in unraveling dynamics of the photoelectron ejection from simple molecules. In order to proceed, it is necessary to examine the photoelectron dipole matrix elements $\langle f | \boldsymbol{\mu}\cdot\boldsymbol{\varepsilon} | i \rangle$ for the photoejection from a bound molecular orbital into a continuum orbital [16,17,34], which is the topic of the next section.

2.1.2 Photoelectron Matrix Element

The dynamics of molecular photoionization are determined by the matrix element of the initial and final state wavefunction connected by the dipole operator, i.e., $\langle f | \boldsymbol{\mu}\cdot\boldsymbol{\varepsilon} | i \rangle$ [3]. The electron is ejected from the initial bound molecular orbital $\phi_i(\mathbf{r})$ into the final photoelectron continuum orbital $\Psi^{(-)}_{f,\mathbf{k}}(\mathbf{r})$ where $\mathbf{k}$ is the momentum of the photoelectron [16,17]. Since the essential feature is the dipole matrix element where the photoelectron state can be described by switching from the laboratory frame to the rotating molecular frame [3], some mathematical formulae need to be developed for the dipole matrix element. The partial wave components $\psi^{(-)}_{klm}$ of the outgoing electron wavefunction $\Psi^{(-)}_{f,\mathbf{k}}(\mathbf{r})$ can be defined by an expansion in spherical harmonics

about **k** where **k** denotes the direction of the momentum in the laboratory frame [16],

$$\Psi^{(-)}_{f,\mathbf{k}}(\mathbf{r}) = \left(\frac{2}{\pi}\right)^{1/2} \sum_{lm} i^l \psi^{(-)}_{klm}(\mathbf{r}) Y^*_{lm}(\mathbf{k}). \tag{2.6}$$

If we transform the final partial wave component $\psi^{(-)}_{klm}$ and the initial partial wave component $\phi_i(\mathbf{r}')$ from the laboratory frame into the rotating molecular frame, then we have

$$\begin{aligned} \psi^{(-)}_{klm} &= \sum_{l'\lambda} g_{lm,l'\lambda}(\mathrm{k},r) \mathcal{D}^{l'}_{m\lambda} Y_{l'\lambda}(\mathbf{r}') \\ \phi_i(\mathbf{r}') &= \sum_{l_0\lambda_0} \phi_{il_0}(r) \mathcal{D}^{l_0}_{\lambda_0} Y_{l_0\lambda_0}(\mathbf{r}'), \end{aligned} \tag{2.7}$$

where m and λ are the projection of l in the laboratory and molecular frame, respectively, and $\mathcal{D}$ is a rotational matrix in Edmonds' notation [16,39]. For the interaction with the polarized light, the dipole momentum can be written [16] in terms of spherical harmonics as :

$$\begin{aligned} \boldsymbol{\mu}\cdot\boldsymbol{\varepsilon} &= e\,\mathbf{r}\cdot\boldsymbol{\varepsilon} \\ &= e\left(\frac{4}{3}\pi\right)^{1/2} \mathrm{r} Y_{1\mu_0}(\mathbf{r}_s), \end{aligned} \tag{2.8}$$

where **r** is the position vector of the electron in the laboratory frame, $\boldsymbol{\varepsilon}$ denotes the polarization vector, and μ_0 specifies the polarization of the light, i.e., $\mu_0 = 0$ for linearly polarized light and $\mu_0 = \pm 1$ for circularly polarized

light propagating along the z axis in the laboratory frame. Next, $Y_{1\mu_0}(\mathbf{r}_s)$ can be transformed into the rotating molecular frame [16].

$$Y_{1\mu_0}(\mathbf{r}_s) = \sum_{\mu} (-1)^{\mu-\mu_0} \mathcal{D}^{(1)}_{\mu_0\mu}(\mathbf{R}) Y_{1\mu_0}(\mathbf{r}'_s), \tag{2.9}$$

where μ is the photon polarization index in the molecular frame. By substituting Eq.(2.9) into Eq.(2.8), the dipole operator can be rewritten as

$$\boldsymbol{\mu}\cdot\boldsymbol{\varepsilon} = e\left(\frac{4}{3}\pi\right)^{1/2} r \sum_{\mu} (-1)^{\mu-\mu_0} \mathcal{D}^{(1)}_{\mu_0\mu}(\mathbf{R}) Y_{1\mu}(\mathbf{r}'_s). \tag{2.10}$$

Using single–center expansions for the photoelectron wave function, the initial orbital and the dipole momentum operator, the partial wave photoelectron matrix elements $r_{fi}^{l\lambda\mu}$ can be defined in the molecular frame for photoionization [16] as

$$r_{fi}^{l\lambda\mu} = \sum_{l',l_0} \left\langle g_{lm,l'\lambda}(\mathrm{k}, r)\, Y_{l'\lambda}(\boldsymbol{r}') \middle| rY_{1\mu}(\boldsymbol{r}') \middle| \phi_{il_0}(r) Y_{l_0\lambda_0}(\boldsymbol{r}') \right\rangle. \tag{2.11}$$

These partial wave photoelectron matrix elements are central to our understanding of the scattering dynamics. Specifically, they play an important role in understanding the dynamical aspect of molecular photoelectron wave functions. In Eq.(2.11), $l \neq l'$ terms arise for the nonspherical fields of molecular systems, while only $l=l'$ terms are allowed for the central fields of atomic systems where the angular momentum for the photoelectron should be

conserved [16,17]. The angular momentum coupling for the nonspherical molecular field occurs due to the torque exerted on the photoelectron during its escape [3,4,17,20]. The partitioning of angular momentum between the photoelectron and ion core is the basis of rotationally resolved studies of molecular photoionization. By examining the photoelectron matrix element, the magnitudes of the partial wave components elucidate the dynamics of the photoelectron ejection. [3,4,16,17].

2.2 Relevant Phenomena in the Ionization Continua

2.2.1 Cooper Minima

In the evaluation of $\langle f | \boldsymbol{\mu}\cdot\boldsymbol{\varepsilon} | i \rangle$, the angular part of the integration proceeds analytically and yields the selection rule on the orbital quantum number of the excited electron [3]. However, in the numerical calculation of the radial matrix element, Eq.(2.12), Cooper [40,41] has shown how the radial wave functions $\phi(r)$ can bring about changes in the absorption cross section,

$$\int_0^\infty dr\, \phi_i(r) r \phi_f(r). \tag{2.12}$$

In the dipole approximation, p electrons can be excited into s- or d-waves due to the selection rule $l = l_0 \pm 1$. The oscillator strength with l_0+1 is generally larger than the one with $l_0 - 1$ [3,4]. The radial wave functions for the Ne($2p$),

Ar($3p$), and Kr($4p$) are shown in Fig. 2.1, along with the radial wave functions for d-waves with zero kinetic energy, i.e., at threshold [40,41]. Since the dipole integral in Eq.(2.12) is influenced by the overlap between the initial p-wave and the final d-wave, Ne has small overlap at $\varepsilon = 0$. But the overlaps for Ar and Kr are negative due to the opposite signs of the wavefunctions. In each case, as the kinetic energy increases, the d-waves move in towards the origin, so the radial integrals begin to change.

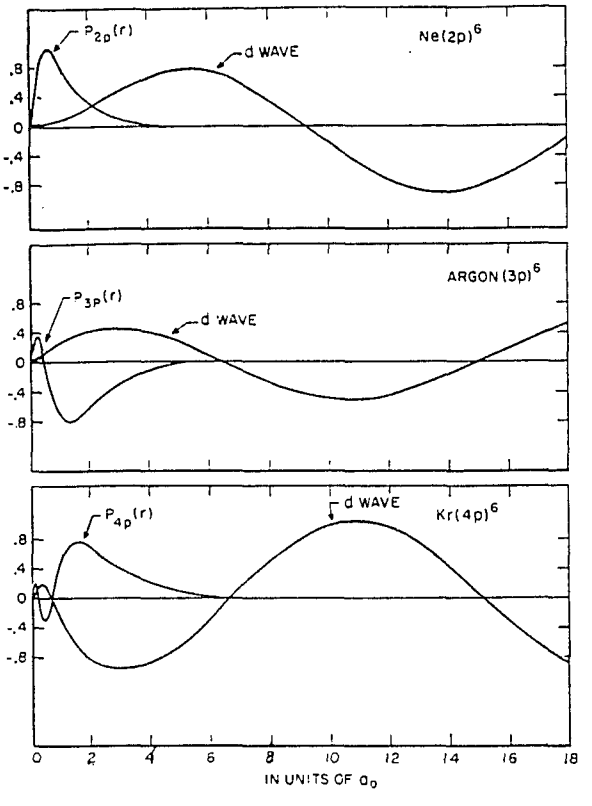

Fig. 2.1 Outer subshell radial wave functions and d waves at zero kinetic energy for Ne, Ar, and Kr from reference [40].

For Ne, the overlap in the dipole integral increases at first and then eventually decreases when the first node of the *d* wave has moved close enough to the origin. On the other hand, for Ar and Kr the overlap is negative at $\varepsilon = 0$ and decreases in magnitude as ε increases, becoming zero when positive and negative portions of dipole integral are equal. Beyond this point, there is a mismatch between positive and negative portions, so the overlap starts to increase as ε increases. The dipole matrix elements for $p \rightarrow d$ transitions are also shown as a function of the kinetic energy in Fig. 2.2 [40,41].

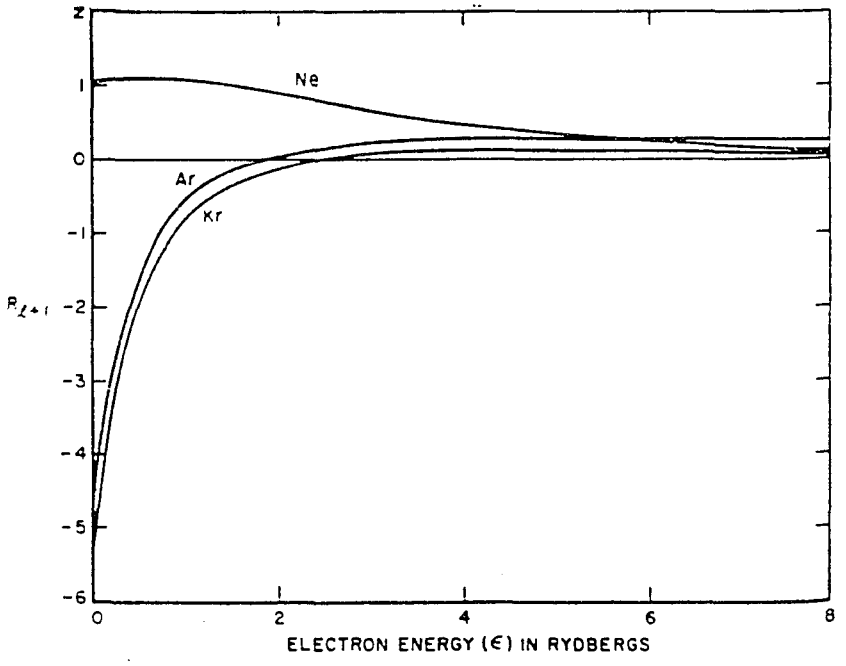

Fig. 2.2 Matrix elements for $p \rightarrow d$ transitions in Ne, Ar, and Kr from [40]

Since the cross section is proportional to the square of the integral in Eq.(2.12), Ar and Kr have zero cross sections at certain kinetic energies. This phenomenon is referred to as a Cooper minimum or a Cooper zero [3,4,40,41]. Cooper also pointed out that cross sections for atomic subshells like Ne($2p$) whose radial wave functions are nodeless (the number of nodes = $n - l - 1 = 0$) do not display such minima [40,41]. For the molecular photoionization, Cooper minima are accompanied by significant angular momentum mixing in the continuum due to the nonspherical molecular potential, and can result in a strong dependence of the rotational distribution as a function of kinetic energy [17].

2.2.2 Shape Resonances

Studies of rotationally resolved molecular photoionization yield insight into the dynamics of resonant photoionization, particularly shape resonant photoionization. This is because shape resonances can strongly influence the rotational motion of the molecular ion [1,2,11]. In order to place my work into context, I will briefly review the barrier penetration description of shape resonances. In this picture, the photoelectron enters a quasibound state in which it is temporarily trapped by a potential barrier, through which it may eventually tunnel and escape [1,2]. Such a quasibound state inside a potential barrier has enhanced electron density in the core region, and one common

cause of the barrier is the angular momentum centrifugal barrier which can block the electron escape in particular directions. Since a centrifugal barrier depends strongly on the angular momentum, shape resonances are frequently associated with particular angular momentum components of the electronic wavefunction [1,2]. For purposes of illustration, it is useful to review a specific example, the well–known σ_u shape resonance in K–shell photoionization of N_2 [42]. The four partial cross sections in Fig. 2.3 represent the four dipole allowed channels in K–shell photoionization of N_2 (the ionization potential is 409.9 eV). In the σ_u partial cross section, an intense and broad peak appears at ~1 Ry above the ionization potential. This effect is caused by a centrifugal barrier acting on the $l = 3$ component of the σ_u continuum wavefunction [1]. The essence of the phenomena can be described as follows. The electric dipole interaction which is localized within the atomic K–shell, produces a photoelectron with $l = 1$. As this p-wave electron escapes into the continuum, the anisotropic molecular field can scatter the electron into the entire range of angular momentum states contributing to the allowed σ and π channels.

In addition, the spatial extent of the molecular field where the separation of the two atoms is 1.1 A, enables the $l = 3$ component of the σ continuum to overcome the centrifugal barrier and penetrate into the molecular core region at the kinetic energy of ~1 Ry. This penetration is rapid, occurring with a

phase shift of ~ π over a range of ~0.3 Ry. These circumstances produce a dramatic enhancement in cross-section, the well–known *f*-wave shape resonance in the σ channel [1]. There is compelling evidence for shape resonance phenomenon for a huge variety of molecules [42].

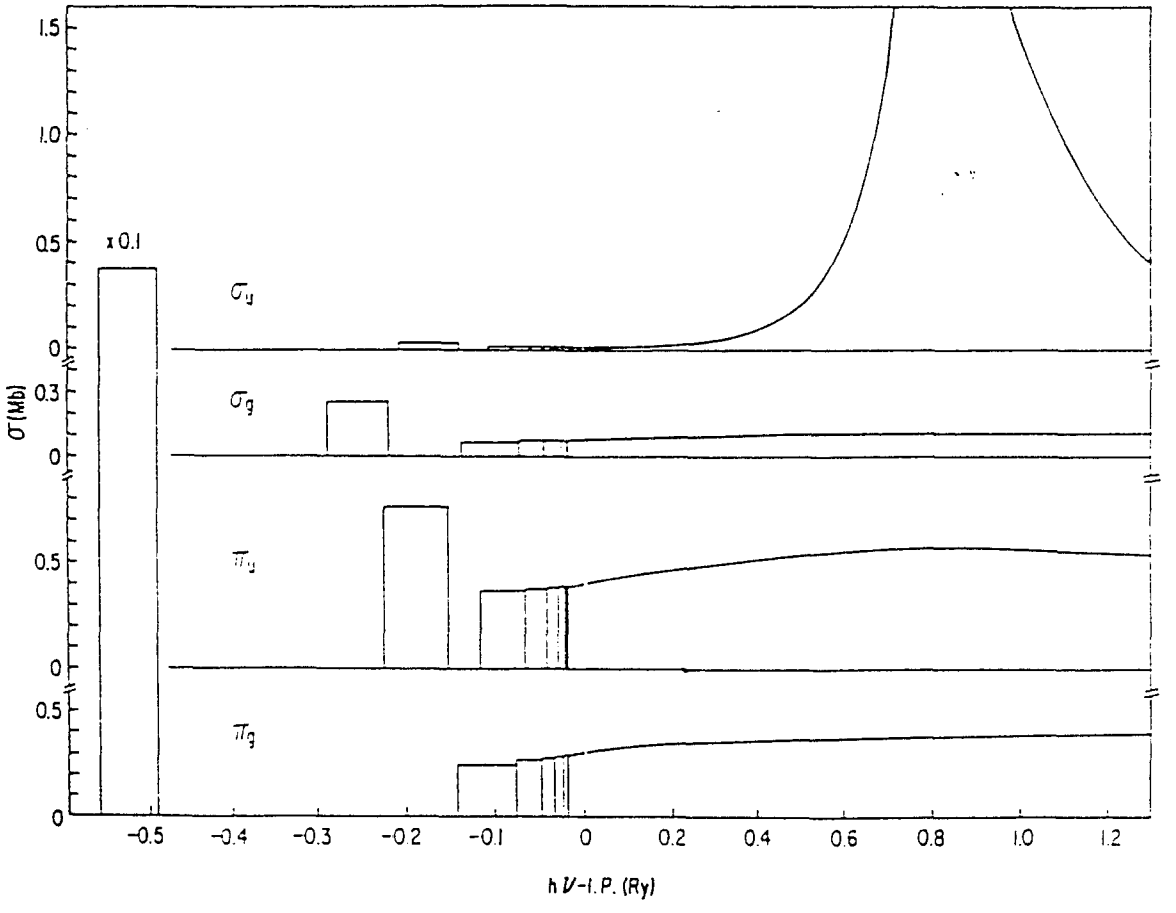

Fig. 2.3 Partial photoionization cross sections for four channels in K–shell photoionization of N_2 from reference [1].

In fact, a monograph on NEXAFS [45] deals primarily with this topic and provides a useful bibliography of molecular systems whose shape resonances have been investigated. I will show how my dispersed fluorescence measurements with rotational resolution provide new insights into this well-documented continuum resonance phenomenon.

2.3 Experimental Background

2.3.1 Dispersed Fluorescence Measurements

Dispersed fluorescence measurements are simple in practice, and serve as one of the methods of studying highly resolved molecular photoionization [6]. The basic idea is that the intensity of fluorescence originating from a particular quantum level of a photoion is proportional to the rate of the production of that level. By exploiting this simple concept, vibrationally or rotationally resolved fluorescence spectra for diatomic or polyatomic molecules can be utilized. To gain a better understanding of the method, it is useful to examine the potential curves for the $2\sigma_u^{-1}$ photoionization of N_2 which are sketched in Fig. 2.4. There are transitions from upper vibrational and rotational levels $v^+= 0, N^+$ of the excited ion state to lower quantum levels $v''= 1, N''$ of the ground ionic state. At the rotationally resolved level of detail, R(N'') branch transitions are assigned for $\Delta N = N^+ - N'' = +1$ while P(N'') transitions are characterized by $\Delta N = -1$ [37].

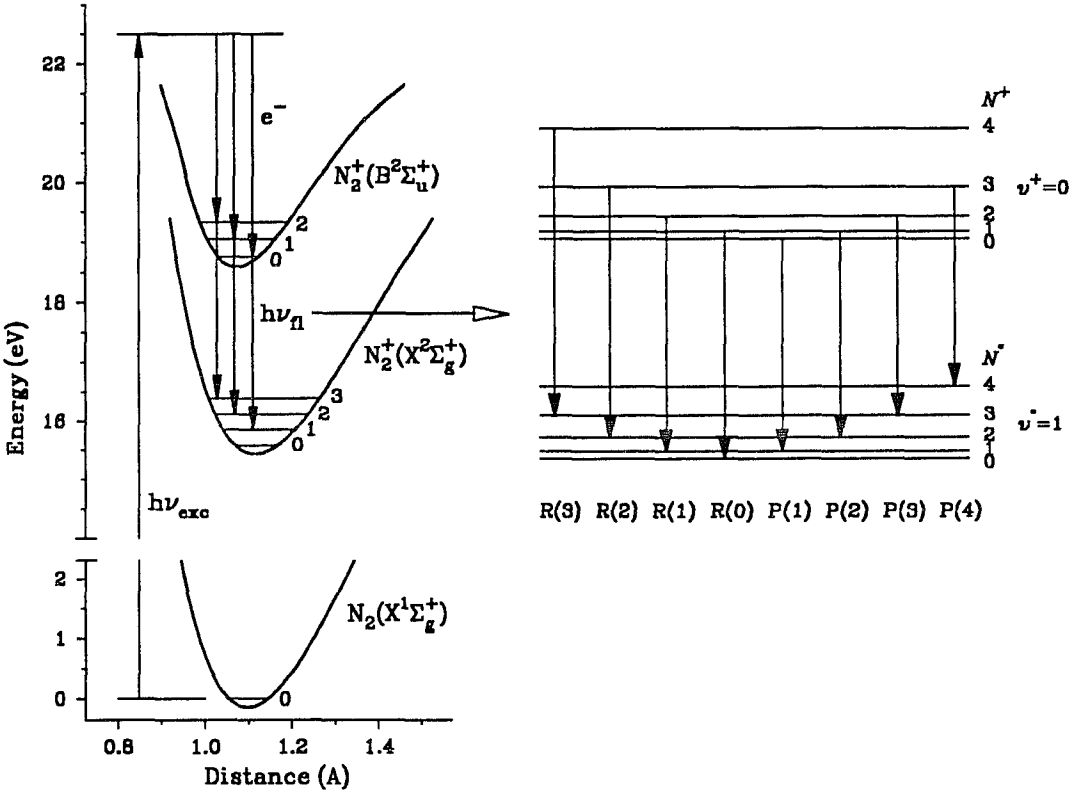

Fig. 2.4 Potential curves for the example of the photoionization of N_2, showing the process for the ionization of N_2 ($X\ ^1\Sigma_g^+$) $\rightarrow$ N_2^+ ($B\ ^2\Sigma_u^+$) and the following fluorescence transition of N_2^+ ($B\ ^2\Sigma_u^+$, $v^+ = 0$, $N^+ \rightarrow$ $X\ ^2\Sigma_g^+$, $v'' = 1$, N'')

In my studies, I measure the intensities of rotational fluorescence transitions originating from the excited photoion state $N_2^+(B^2\Sigma_u^+, v^+ = 0, N^+)$. This figure indicates that it is possible to determine the relative populations of the corresponding rotational levels denoted by N^+. Synchrotron radiation ionizes the neutral N_2 target molecules, creating the

fluorescing $N_2^+(B^2\Sigma_u^+, v^+=0, N^+)$ state when $h\nu_{exc}$ exceeds the ionization potential (I.P.= 18.757 eV [44]). The excitation-fluorescence sequence is given in Eq.(2.13) [6]

$$N_2(X^1\Sigma_g^+,\ v_0=0,\ N_0) + h\nu_{exc} \rightarrow N_2^+(B^2\Sigma_u^+,\ v^+=0,\ N^+) + e^-$$

$$\downarrow$$

$$N_2^+(X^2\Sigma_g^+,\ v''=1,\ N'') + h\nu_{N^+N''}. \qquad (2.13)$$

The fluorescence intensity $h\nu_{N^+N''}$ originating from the $N_2^+(B^2\Sigma_u^+,\ v^+, N^+)$ level is a measure of the rate of the production of that level, i.e., its partial photoionization cross section [32].

From the previous discussion, it is clear that the information content from dispersed fluorescence spectroscopy is similar to that of photoelectron spectroscopy [4]. However, there are qualitative differences between the two techniques [6]. I list advantages of fluorescence spectroscopy that play a crucial role in my studies, but preclude the use of photoelectron spectroscopy.

- The fluorescence detection bandwidth is determined by the bandwidth of the optical system used in the fluorescence channel. Therefore it is not related to, or limited by, the excitation bandwidth. As a result, highly resolved data can be obtained on the photoions by optimizing the conditions of the optical monochromator even when the excitation

bandwidth becomes broad. This is the most important instrumental characteristic of the fluorescence measurements. This technical advantage of the fluorescence spectroscopy makes the study of the highly resolved photoionization feasible regardless of the bandwidth of the excitation energy. Fig. 2.5 shows the experimental strategy for the fluorescence method versus photoelectron spectroscopy. When the synchrotron radiation bandwidth is broad, the electron energy resolution is not adequate for rotational resolution. However, the fluorescence bandwidth is decoupled from the excitation bandwidth and depends only on the optical system.

- High resolution studies of photoelectron spectroscopy are limited to threshold, or near-threshold photoionization phenomena. On the other hand, dispersed fluorescence measurements can provide the vibrational as well as rotational resolution over a broad excitation energy well beyond the reach of existing electron energy analyzer technology where the resolution depends on electron kinetic energy.

- External electric and magnetic fields can be used for fluorescence studies [43], while such perturbations either degrade or preclude photoelectron spectroscopy studies. The external fields easily influence photoelectron spectroscopy studies of near–threshold photoionization where the photoelectron has the low kinetic energy.

- The collection efficiency for the fluorescence monochromator is typically higher than the efficiency for electron spectrometers [32].

Fluorescence vs. electron detection

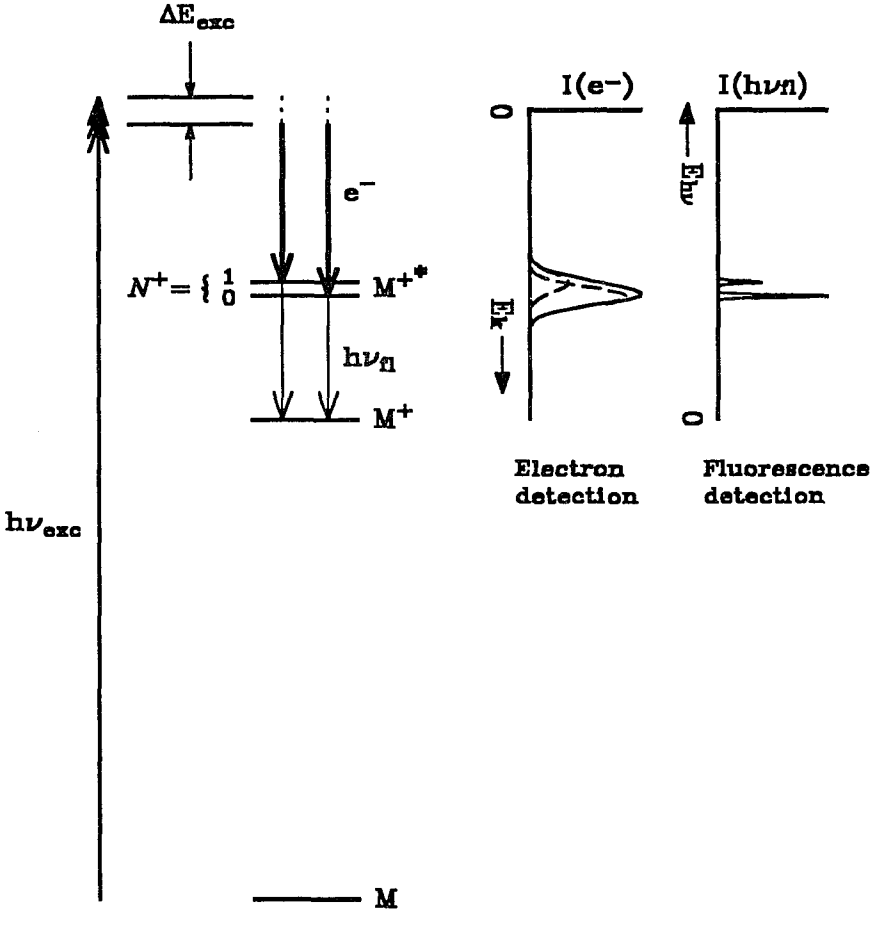

Fig. 2.5 The experimental strategy for the fluorescence measurement versus the photoelectron spectroscopy with the broad bandwidth of tunable synchrotron radiation.

Moreover, higher sample pressures can be used in fluorescence measurements as long as secondary electron scattering processes do not introduce artifacts. However, higher sample pressures degrade electron

spectroscopy measurements owing to electron scattering of the photoelectrons.

Although the above features provide compelling reasons to perform fluorescence spectroscopy measurements, some of them can serve as limitations under certain circumstances. These are listed below [6].

- By definition, studies using fluorescence spectroscopy are restricted to excited states that fluoresce. Many excited states of ions decay via fragmentation rather than fluorescence [5]. Therefore, dispersed fluorescence measurements limit the selection of available samples.
- Because the fluorescence bandwidth is uncoupled from the excitation bandwidth, it can be possible that the excited ionic state of interest is not exclusively created by direct photoionization, but by the production of more highly excited ionic states followed by fluorescence cascades. While this is perhaps the most daunting problem in principle, it is not usually observed in practice for molecular systems [47].
- The analysis of fluorescence results can be complicated by the ionization induced by secondary electrons ejected from the primary photoions. This can be evaluated experimentally, however.

As the above remarks indicate, there is a complementarity between dispersed fluorescence spectroscopy and photoelectron spectroscopy. For studies at lower photon energies, photoelectron spectroscopy is more acceptable while

fluorescence spectroscopy is preferable for studies over a broader energy range [6]. We compare results of vibration branching ratios for N_2O, which are obtained from the two methods, i.e., dispersed fluorescence and photoelectron spectroscopy in Fig. 2.6.

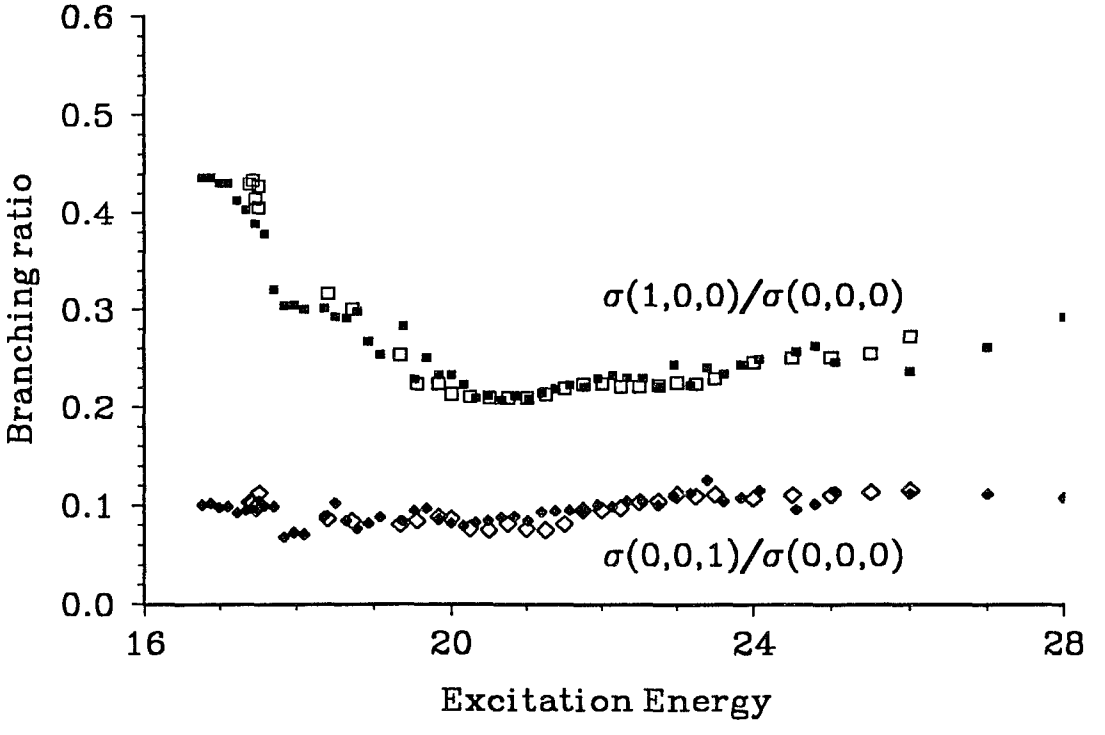

Fig. 2.6 Comparison of dispersed fluorescence spectroscopy [46] and photoelectron spectroscopy [47] for the vibrational branching ratios of N_2O from reference [6].

For this fluorescence study on N_2O [46], there was a complementary photoelectron investigation which generated photoelectron asymmetry parameters and vibrational branching ratios at the lower excitation energies [47]. Clearly, these vibrational branching ratios are in excellent agreement for the two methods, and give us confidence that dispersed fluorescence spectroscopy can be exploited effectively for even more highly resolved studies, and in particular, for the rotationally resolved work which is the goal of this thesis project.

2.3.2 Excitation / Emission Model

In order to analyze fluorescence results from photoions quantitatively, it is useful to recognize that the process is naturally broken into two parts. First is the excitation from the neutral ground state to the ionic excited state, and this is followed by the fluorescence from the excited to the ground ionic state. To predict the photoion rotational distribution from the measured fluorescence intensity, it is necessary to interpret the excitation as well as the fluorescence transitions. The diagrams of the excitation followed by fluorescence transition are sketched in Fig. 2.7.

The rotational transition of the ionic state N_2^+ ($B^2\Sigma_u^+$,v^+,N^+) from the N_2 ($X^1\Sigma_g^+$) ground state is first outlined as follows. Both the N_2 ($X^1\Sigma_g^+$) and N_2^+ ($B^2\Sigma_u^+$) are Hund's case (b) because the component of the

electronic orbital angular momentum along the internuclear axis is $\Lambda = 0$ and the spin vector S is only very weakly coupled to the internuclear axis [37].

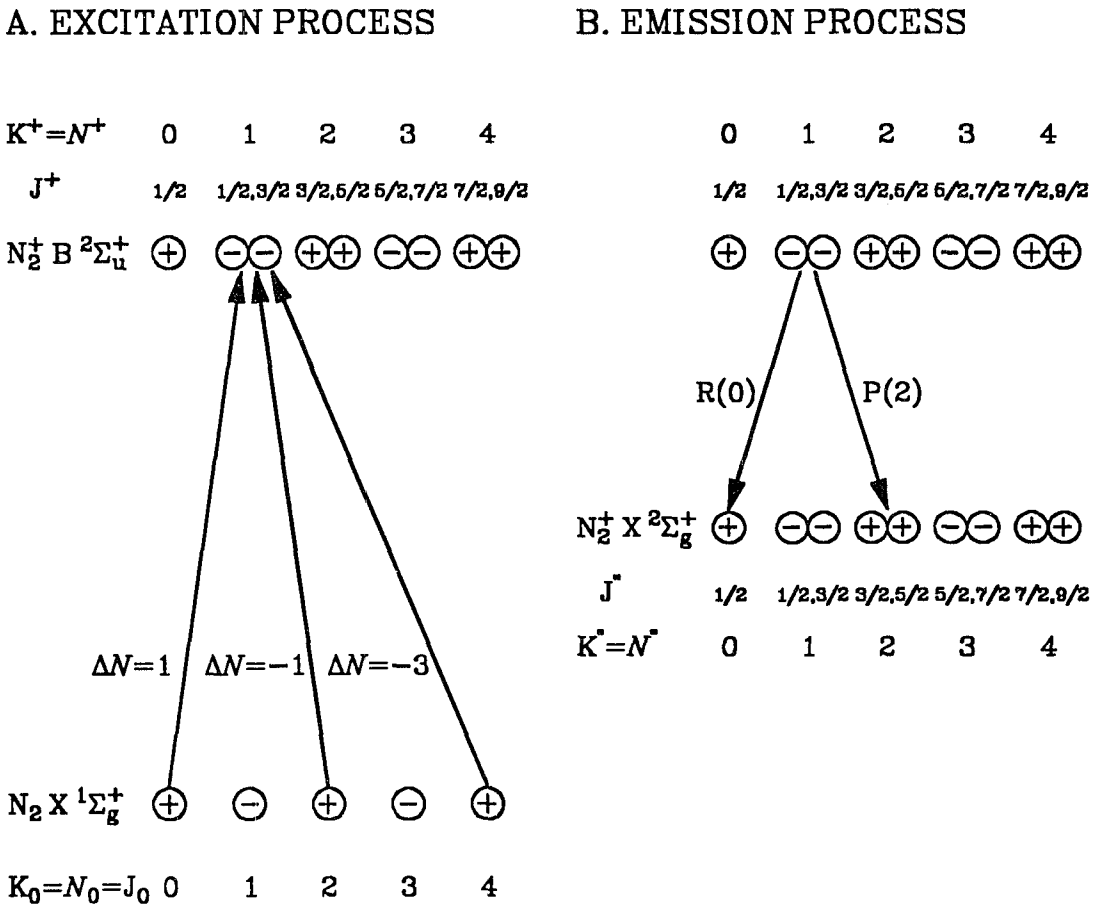

Fig. 2.7 **A.** The excitation process of the rotational transition from the N_2 ($X\ ^1\Sigma_g^+$) state to the N_2^+ ($B\ ^2\Sigma_u^+$) state. **B.** The emission process of the rotational transition from the N_2^+ ($B\ ^2\Sigma_u^+$) state to the N_2^+ ($X\ ^2\Sigma_g^+$) state.

The rotational energy levels are then designated by the total angular momentum apart from spin K ($\equiv N$) that can have the values of K = Λ, Λ + 1, Λ + 2, ... In addition, the positive and negative rotational levels in Fig. 2.7 can be distinguished by whether the total eigenfunction remains unaltered or changes sign by reflection of all the particles at the origin [37]. As a result, the even rotational levels for Σ^+ states are positive. For the central fields of the atomic system, the selection rule for the $\Sigma^+ \rightarrow \Sigma^+$ transition is $\Delta K = \pm 1$ with $\Delta K = 0$ being forbidden and the positive levels combined only with the negative ones, i.e., $+ \leftrightarrow -$ [37]. However, for the nonspherical fields of the molecular system, $\Delta K (\equiv \Delta N) = \pm 3, \pm 5, \ldots$ as well as $\Delta N = \pm 1$ are possible during the escape of the photoelectron [17,31]. For the dipole-dominated $^1\Sigma_g^+ \rightarrow {}^2\Sigma_u^+$ transition in diagram A of Fig. 2.7, the rotational level N^+ of the N_2^+ ($B^2\Sigma_u^+$) state is most populated by the selection rules ($\Delta N = \pm 1$, and $+ \leftrightarrow -$) from the rotational levels $N_0 = N^+ - 1$ and $N^+ + 1$ of the $N_2(X^1\Sigma_g^+)$ state [48–50]. Assuming that the $N_2(X^1\Sigma_g^+)$ target rotational population distribution has a Boltzmann distribution, the rotational population n_{N_0} of the neutral ground state can be estimated by a rotational temperature T_0 [48–50], i.e.,

$$n_{N_0} = C \cdot (2N_0 + 1) \cdot \exp\{-B_{v_0} N_0 (N_0 + 1) hc / kT_0\}, \qquad (2.14)$$

where C is a constant, k is the Boltzmann constant, and the rotational constant B_{V_0} in the vibrational state v_0 is calculated by $B_{V_0} = B_e - \alpha_e(v_0+½)$, where rotational constants B_e and α_e for the N_2 ($X^1\Sigma_g^+$) state are 2.010 and 0.0187 cm^{-1}, respectively [37]. Even at room temperature, there is no significant excitation of vibrational levels other than $v_0 = 0$. So, we focus on the rotational transition by neglecting the vibrational transitions in the following discussion.

At this juncture, a brief digression is in order. There have been attempts to estimate the ionic populations using a model that simplifies the scattering process [37]. We will find that this estimate is not accurate, and that it is in fact an oversimplification. I will cover it here for completeness. Once we obtain the rotational distribution of the N_2 ($X^1\Sigma_g^+$) target state from Eq.(2.14), it is possible to estimate what the the population n_{N^+} would be if the scattering dynamics are neglected, and treated in a pure case (d) limit. The expression obtained for this limiting case is

$$n_{N^+} = K \cdot \left\{ n_{N_0=N^+-1} \cdot P_{\Delta N=1} + n_{N_0=N^++1} \cdot P_{\Delta N=-1} \right\}, \qquad (2.15)$$

where K is a constant and the rotational transition probabilities P are normalized Hönl-London factors for the $\Delta\Lambda = 0$ transition given in terms of N^+ [37,48] as :

$$P_{\Delta N=1}=\frac{N_0}{2N_0+1}=\frac{N^+ +1}{2N^+ +3} \qquad \text{for } N^+ - N_0 = 1$$

$$P_{\Delta N=-1}=\frac{N_0+1}{2N_0+1}=\frac{N^+}{2N^+ -1} \qquad \text{for } N^+ - N_0 = -1. \qquad (2.16)$$

These expressions do not depend on the photoelectron kinetic energy, and we will find that they do not approximate the observed behavior in even a qualitative sense. In the application of this excitation model, the dipole selection rule ΔK ($\equiv \Delta N$) = ± 1 was assumed [48–50]. However, due to the photoelectron sampling the molecular field, the partitioning of angular momentum between ion and photoelectron permits transitions of $\Delta N = \pm 1, \pm 3, \pm 5, \ldots$ in molecular photoionization. It will be necessary to use a more realistic picture than this simple excitation model [48]. In order to go further, we need experiments to extract ionic populations, and realistic scattering calculations to estimate the actual behavior. First, we will review the strategy for determining the ionic rotational populations.

In order to estimate the true ionic populations, i.e., the n_{N^+}, it is necessary to relate the observed rotationally resolved emission intensities, $I_{N^+N''}$, with the rotational populations. For the emission process sketched in diagram B of Fig. 2.7, we develop the relationship between n_{N^+} and $I_{N^+N''}$ by starting with the intensity of a general emission band [37,48], i.e.,

$$I_{N^+N''} = a(\nu)\, h c \nu, \qquad (2.17)$$

where a(ν) is the rate of photon emission and ν is the wave number of the emission. Since the rate of fluorescence from rotational level N^+ is proportional to the rate of the excitation to that level, the rate of the photon emission can be expressed as :

$$a(\nu)_{N^+N''} = K \cdot n_{N^+} \cdot P_{N^+N''} \cdot \nu^3, \qquad (2.18)$$

where K is constant and $P_{N^+N''}$ represents the rotational transition probability, so that $P_{N^+N''} = \frac{N^+}{(2N^+ + 1)}$ is for the R–branch ($\Delta N = N^+ - N'' = 1$) of the $\Delta\Lambda = 0$ transition and $P_{N^+N''} = \frac{(N^+ + 1)}{(2N^+ + 1)}$ is for the P–branch transition ($\Delta N = -1$) [37,48]. By combining Eqs.(2.17) and (2.18), a simple relation between the emission intensity and the rotational population is established as follows .

$$I^{em}_{N^+N''} = K \cdot n_{N^+} \cdot \frac{N^+}{(2N^+ + 1)} \cdot hc\nu^4 \qquad \text{for R–branch transition}$$

$$= K \cdot n_{N^+} \cdot \frac{(N^+ + 1)}{(2N^+ + 1)} \cdot hc\nu^4 \qquad \text{for P–branch transition,} \qquad (2.19)$$

where the factors N^+ and $N^+ + 1$ are from the Hönl–London formulae for the $\Delta\Lambda = 0$ transition [37,48]. We will use the relations in Eq.(2.19) to determine the populations of each rotational level for the $N_2^+(B^2\Sigma_u^+)$ state from the measured fluorescence intensities.

CHAPTER III.

EXPERIMENT

3.1 Synchrotron Radiation from CAMD–PGM

The synchrotron radiation used in this work originates from the electron storage ring at the Center for Advanced Microstructures and Devices (CAMD). This facility was established in 1988 at Louisiana State University in Baton Rouge, and is described in detail elsewhere [51]. The radiation from this facility is monochromatized by a 6m plane grating monochromator (PGM) [52]. This PGM beam line was first operated in 1993 and was designed for a variety of uses. Specifically, it can cover a very wide spectral range, and can be utilized in different operating modes depending on the experimental needs. The available modes of operation include high resolution, high throughput, and high order rejection modes [52]. Synchrotron radiation in the spectral range from approximately 10 eV to 1200 eV can be covered by two gratings (interchangeable in vacuum). The low energy grating has 360 grooves/mm and the high energy grating has 1220 grooves/mm. The optical elements and layout of the PGM are shown in Fig 3.1. The diverging radiation is collimated in the horizontal plane by the cylindrical collimating mirror and focused in the vertical plane by the vertical mirror (also cylindrical). The vertical focus is the entrance slit of the monochromator. After the slit, the radiation passes

through a four jaw aperture to a plane premirror that translates and rotates. The premirror can be adjusted so that the angle on the grating can be varied as an additional degree of freedom. This allows the monochromator to be operated in three modes, the fixed focus mode, the high order rejection mode, or the high throughput mode [52]. The radiation selected by the grating is diffracted to a spherical mirror that focuses the radiation on the exit slit. The radiation that passes through the exit slit is focused into the experimental chamber by a toroidal refocusing mirror.

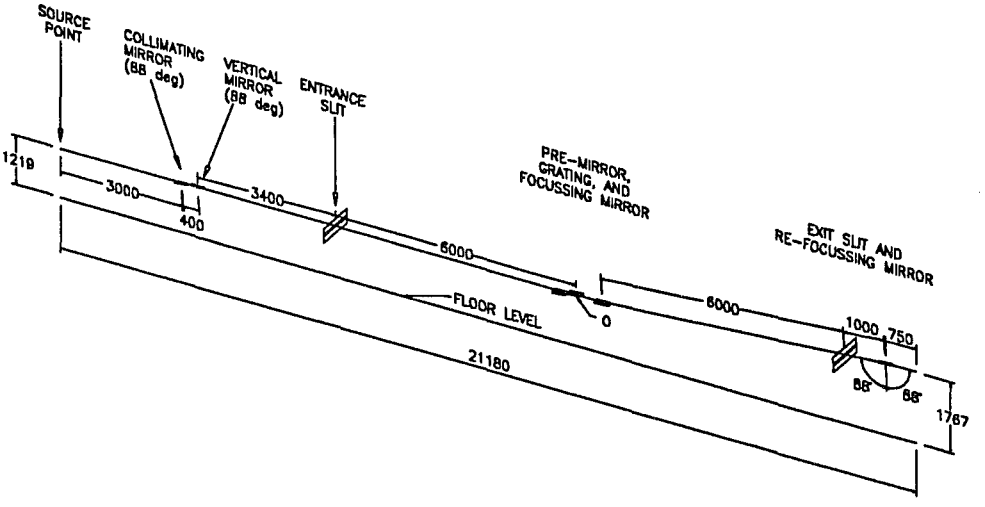

Fig. 3.1 Optical layout of the PGM beam line. Distances are in mm.

During our measurements, we operate the monochromator in the high throughput mode where the premirror maintains an angle of incidence such that the grating operates near its blaze angle. For rotationally resolved fluorescence measurements, the photon energy is selected in the range of 20 eV to 220 eV using the low energy grating at 5 different premirror angles (77.1°, 77.5°, 80°, 82°, and 85°). Downstream from the refocusing mirror at the end of the beam line is a pneumatic gate valve with a glass window in the gate. Following this is the experimental apparatus, a molecular beam apparatus with high pumping speed and an optical system for detecting the intensity of dispersed fluorescence. The pneumatic gate valve is interlocked to an ion gauge to safeguard the ultrahigh vacuum of the beam line.

The incident photon flux can be measured by the tungsten mesh before the experimental chamber and also by the Al_2O_3 photodiode mounted on the end of the beam. A picoammeter that is connected to the cathode of the photodiode is used to read the rate of the emission of low-energy electrons from the photocathode. The picoammeter also provides a voltage output that is proportional to the current, and the output is fed into a voltage-to-frequency (V / F) converter. The photodiode signal that is proportional to its voltage input is counted by a CAMAC Hex Scaler (Kinetic System, Module 3615) and stored by the computer. Even though many factors affect the incident photon flux, the typical reading of the picoammeter is ~10 nA during

our experiment. From this current, the incident flux of the beam is estimated [6,7] :

$$10 \cdot 10^{-9}\ A = 10^{-8}\ C/s = 10^{-8}\ C/s \ / (1.6 \times 10^{-19}\ C/e^{-}) = 10^{11}\ e^{-}/s. \quad (3.1)$$

Since the quantum efficiency of the photodiode is approximately 10 %, i.e., one electron is detected for 10 incident photons on the photocathode, the number of photon per second for the incident beam is approximately 10^{12} hν/s in the high throughput mode with beam currents of 100 mA in the electron storage ring (1.3 GeV beam energy). Once the incident intensity is measured, all data are normalized to a constant value of the incident flux. In order to characterize the performance of this new PGM beam line, higher order contributions and effects are estimated using metal foil filters. Higher order contributions to photoionization depend on their strength and the photoionization cross section of sample at their energies [53]. The results of my study were identical within experimental error with or without Sn and Al filters in the energy range (19 eV $\leq h\nu_{exc} \leq$ 75 eV). This is probably because the ionization cross sections are decreasing rapidly with energy, negating serious complications from higher order contributions. Furthermore, by measuring the energy positions of the Al L–edge threshold cut–off (zero–, first–, and second–order) with the Al filter in place, we were able to calibrate the excitation energy. Also, we estimated the excitation bandwidth by

measuring the width of the L–edge threshold for the Al filter. As a result, the bandwidth at the photon energy 30 eV is estimated as ~1 eV when the entrance and exit slits of the PGM are fully opened.

3.2 Photoionization End–station

3.2.1 Layout

Synchrotron radiation from PGM beam line is introduced into the region of the interaction by two capillary tubes. The main chamber is isolated from the ultra high vacuum beam line by this two-stage differential pumping region, so that the pressure of the intermediate chamber between the beam line and the main chamber is kept at $\sim 10^{-9}$ Torr by pumping with a 50 L/s turbopump after the first stage and a 170 L/s turbopump (Balzers, TPU 170) after the second stage. To obtain this low pressure, the intermediate chamber is baked at the temperature of ~ 40° C for at least 10 hours. The ion gauge controller (Granville Phillips, Series 270) monitors the intermediate chamber pressure and links with the pneumatic gate valve to close if pressure rises higher than the set point ($\sim 2\times 10^{-8}$ Torr). Two capillary tubes link the intermediate chamber to the main chamber and channel the incident radiation. The separation of two capillary tubes is ~1/8 inch and the space is pumped by a 50 L/s turbo pump (Balzers, TPU 50), so that the gas flow from the main to

the intermediate chamber is greatly reduced. Furthermore, since two capillary tubes of the 2 mm inner diameter have the low conductance $\sim 3 \cdot 10^{-3}$ L/s in transmitting the gas [7], only few gas molecules are able to reach the intermediate chamber. The incident radiation through the tubes is aligned to intersect the molecular beam so that the region of interaction lies at the focus of the collimating lens inside the main chamber. We are also able to see the beam spot (~0.01 cm^2) on the sodium salicylate screen attached at the pin guide which is mounted on the linear motion feedthrough. The main chamber is pumped by a 2500 L/s cryopump (CTI CryoTorr 10) and is normally maintained at $\sim 8 \times 10^{-4}$ Torr during the experiments. The sample pressure in the region of the interaction is estimated to be about a factor of 40 greater than the chamber pressure, or $\sim 3 \times 10^{-2}$ Torr. This sample pressure corresponds to a number density $N \approx 10^{15}$ cm^{-3} according to the gas law :

$$N = n \cdot N_A / V = (P \times N_A) / (R \times T) \approx 10^{15} \text{ cm}^{-3}, \qquad (3.2)$$

where P is the pressure, R is the gas constant (0.0821 L·atm / mol·K), N_A is Avogadro's constant (6.022×10^{23} mol^{-1}), and T is the temperature. The sample molecules are introduced into the chamber through an interchangeable orifice of the gas–jet assembly mounted on an XYZ manipulator. For this study, a 50 μm diameter aperture disc is used, and the stagnation pressure behind the aperature is set to 250 psig to rotationally cool the target

molecules. The coldest spot can be found by adjusting the gas–jet. For this rotationally resolved photoionization study, we used diatomic gases, N_2 and CO which are commercially obtained and are of ultra high purity.

3.2.2 Optics

For the optical alignment of the monochromator, we use a He–Ne laser to scatter radiation off a pin mounted on a linear feedthrough placed at the interaction region. The optical schematic is sketched in Fig. 3.2.

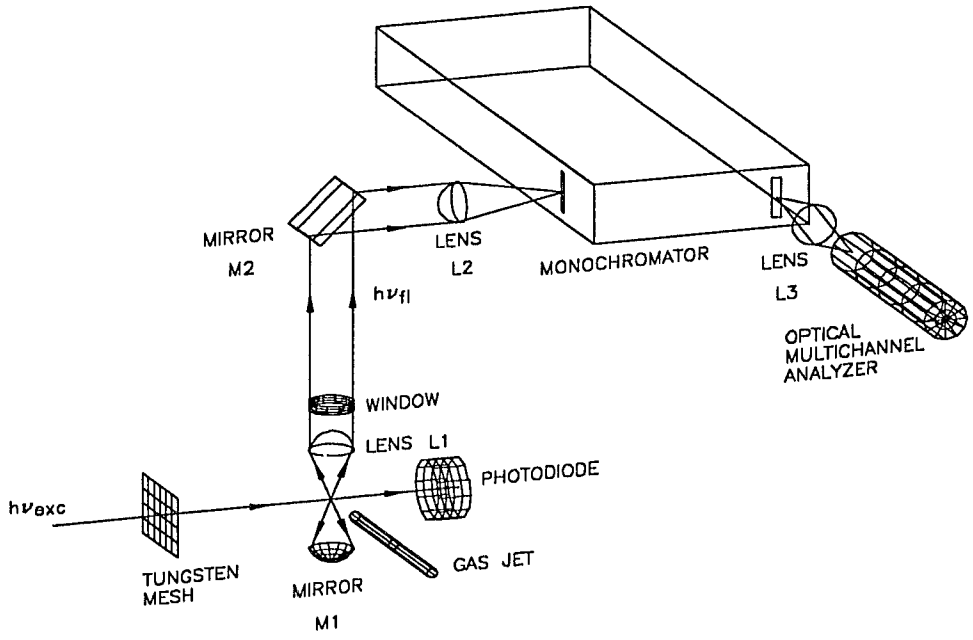

Fig. 3.2 Experimental schematic showing the optical path.

The scattered radiation is collected by a plano–convex lens L1 (focal length f = 100 mm and dia. = 25 mm). The signal is nearly doubled by a concave mirror M1 (f = 100 mm, dia. = 25 mm) that is placed below the region of interaction, and reflects the downward radiation to lens L1. The collimated radiation passes through a window and is deflected by a 50 mm × 50 mm square mirror M2. An f = 125 mm, dia. = 25 mm plano–convex lens L2 focuses the deflected radiation on the entrance slit of the optical monochromator (Instruments SA, THR 1000). Inside the monochromator, the diverging light is deflected by a plane steering mirror, then reflected onto the holographic grating by a collimating mirror. The focusing mirror has 1 m focal length, and focuses the dispersed radiation on the exit slit (or the exit plane, in the case of multichannel detection). Up to this point, we complete the optical alignment of the monochromator with the visible image of the He–Ne laser, then a low pressure Hg lamp is used for the alignment of the detector, an optical multichannel analyzer, or OMA. The Hg lamp is used because it provides radiation closer to the wavelength of the true signal. This is important because chromatic aberration can be significant in determining the best placement of the lens L3. The radiation diverging after the exit slit is focused onto the photocathode of OMA (diameter of active area is 25 mm) by an f = 100 mm, dia. = 50 mm plano–convex lens L3 that is placed between the monochromator and the detector. For rotational fluorescence measurements

of N_2 and CO, we install a 3600 grooves/mm grating in the optical monochromator where its corresponding wavelengths are set at 4275 Å and 2300 Å, respectively. The reflectivity of the grating is 35 %. The reciprocal linear dispersion is 1.5 Å/mm at 4275 Å and 28 % and 2.4 Å/mm at 2300 Å. Since the detection bandwidth is uncoupled from the excitation bandwidth, the rotational resolution depends solely on the entrance slitwidth of this monochromator and the dispersion of the grating. In order to optimize for the collection of the light, the entrance slit width of the monochromator is set 300 μm for N_2 and 80 μm for CO, resulting in bandwidths $\Delta\lambda$ of 0.45 Å and 0.2 Å, respectively. The high spatial resolution detector combined with the high dispersion of the grating makes it possible to resolve rotationally even the CO^+ fluorescence. All lenses and windows are chosen to be fused-silica for high transmittance (~90 %) over a broad spectral range. The mirrors are MgF_2–coated Al (reflectance ~90 %). We estimate the final optical detection efficiency η_{det} by separating the collection efficiency η_{col} and the transmission efficiency η_{tra}. The collection efficiency η_{col} of the lens L1 is the ratio of the corresponding solid angle Ω of the lens L1 to the maximum solid angle 4π, so $\eta_{col} = \Omega/4\pi$. For the dia. = 25 mm and f = 100 mm lens L1, the solid angle Ω is given $4\pi\ (1-\cos\theta)$, where $\theta = \tan^{-1}(12.5/100)$, and the collection efficiency is nearly doubled by the mirror M1. Therefore, the collection efficiency becomes [7]

$$\eta_{col} = 2\times[2\pi(1-\cos\theta)] / 4\pi \approx 0.8\ \%. \qquad (3.3)$$

The transmission efficiency η_{tra} is estimated from three factors; ~50 % transmitted photons ε_{opt} through the lenses and mirrors, ~30 % reflection efficiency ε_{gra} of the grating, and 10 % quantum efficiency ε_{det} of the photocathode of OMA. Thus,

$$\eta_{tra} = \varepsilon_{opt} \times \varepsilon_{gra} \times \varepsilon_{det} \approx 1.5\ \%. \qquad (3.4)$$

The net detection efficiency η_{net} is estimated as the product of the collection efficiency η_{col} and the transmission efficiency η_{tra}. So, we have

$$\eta_{net} = \eta_{col} \times \eta_{tra} \approx 0.012\ \%. \qquad (3.5)$$

This net detection efficiency is used in estimating the net count rate in the next chapter.

3.2.3 Detector

The rotationally resolved dispersed fluorescence spectra are obtained by the optical multichannel analyzer detector. For the purposes of these studies, this detector was far superior to a single-channel photomultiplier detector. This OMA (Quantar Technology, Model 2601A) provides superior single photon counting detection with a high signal/noise ratio, and generates data

much more efficiently than single channel detection. First of all, it reduces the data acquisition time because fluorescence intensities are simultaneously measured for an entire spectral range. In addition, it has the advantage that the background level per unit wavelength interval is much lower than for the photomultiplier. In operation, photons on the photocathode generated photoelectrons which are accelerated toward the first multichannel plate (MCP). By subsequent electron multiplication, the amplified electronic charge packet is deposited on the anode, where it diffuses toward four corner-located electrical collection contacts. The proportion of the total charge from each event is measured and recorded as the XY position. For rotational resolution, we used 10 bit (1024 channels) digital output that has low dark count, typically less than 0.04 count per sec per channel. Over the 25 mm field view, the imaged wavelength range is 1.5 Å/mm (the dispersion of the 3600 grooves/mm grating at 4300 Å) × 25 mm = 37.5 Å for N_2, and 2.4 Å/mm × 25 mm = 60 Å for CO. The detected signals by OMA interfaced with a position computer (Model 2401A) are stored in an AT–386 personal computer. The counting rate detected by OMA can be estimated to illustrate the experimental capabilities for the measurements. The number of excited state ions formed per second I_{exc} is known as the product of four factors [6,7].

$$I_{exc} = I_0 \times N \times \sigma \times l, \qquad (3.6)$$

where the incident intensity I_0 is estimated as 10^{12} hν/s, and the number density N of target molecules at the sample pressure $3 \cdot 10^{-2}$ Torr is estimated in Eq.(3.2) as 10^{15} cm^{-3}. The cross section for N_2 $2\sigma_u^{-1}$ photoionization is ~2 Mb (2×10^{-18} cm^2) [56], and the pathlength is estimated as ~0.2 cm. So, the excitation rate I_{exc} is on the order of 4×10^8 Hz. Due to the net detection efficiency $\eta_{net} \approx 0.012$ % from Eq.(3.5), the net fluorescence count rate I_{net} is estimated as

$$I_{net} = I_{exc} \times \eta_{net} \approx 10^4 \text{ Hz.} \qquad (3.7)$$

The OMA background rate per unit wavelength interval is much lower than that of a photomultiplier, and is typically the limiting factor in determining the data quality for weak signals to be required extremely high resolution. For the cooled channel plate of OMA, the dark count rate integrated over the total area of the detector (≈500 mm^2) is less than 150 Hz. This implies an effective dark count rate of 0.03 Hz, considering the area of observation for the particular transition as 0.05 mm×2 mm (0.1 mm^2). With such the low dark count, the relative uncertainty in the net signal can be estimated as : [6,7]

$$\frac{\Delta S_{net}}{S_{net}} = \frac{\sqrt{[\Delta S_{tot}]^2 + [\Delta S_{back}]^2}}{S_{tot} - S_{back}} = \frac{\sqrt{S_{tot} + S_{back}}}{S_{tot} - S_{back}}, \qquad (3.8)$$

where the net signal $S_{net} = S_{tot} - S_{back}$ represent that the background signal is subtracted from the total signal (signal plus background). Eq.(3.8) is used to determine the statistical uncertainty in data. The above result is also useful for estimating the accumulation time for obtaining data of a given relative uncertainty. If we deal with an extremely weak channel with an OMA signal rate 1 Hz with a dark count rate of 0.03 Hz, it would take approximately 1/2 hour to obtain the data with the relative uncertainty ($\Delta S_{net}/S_{net}$) less than 2.5 %. However, a photomultiplier might have the same true signal rate of 1 Hz, but a typical background rate would be ~ 5 Hz. Using the analysis above, it is straightforward to show that it would require over 5 hours to obtain a single data point with the comparable statistical quality [6,7]. Due to the smaller uncertainties in data and the shorter accumulation time, the OMA makes possible studies of rotationally resolved measurements that would otherwise be out of reach.

3.2.4 Data Acquisition

The fluorescence spectra dispersed by the optical monochromator are measured with the OMA interfaced to a position computer. The position computer detects an event and determines its XY coordinate location. The main electronics controller provides the upper and lower level discriminator as well as the digital output. By using the 10 bit digital output, X and Y

analog position signals are digitized into 1024 × 1024 channels (spatial position data points) in both X and Y dimensions. With the electronic window of the position computer, 2–D electronic active area can be selected from the entire physical active area of sensor. That allows us to exclude unwanted areas from the output or select the portion of the image for output. With the high spatial resolution and ultra low dark count of OMA, the dispersed fluorescence spectra are obtained for various excitation energies. At the same time, the photodiode signal during the accumulation time is collected by a CAMAC scaler (Kinetic Systems, Module 3615) interfaced to the computer because the Al photodiode is used to monitor the intensity of the excitation energy. Since the intensity of the fluorescence transition is regarded as the area under the spectra peak, the intensity of each corresponding fluorescence peak is numerically integrated.

CHAPTER IV.

RESULTS AND DISCUSSIONS

4.1 Overview

Rotationally resolved molecular photoionization data probe the angular momentum composition of the photoelectron and the partitioning of the angular momentum between the photoelectron and ion core [3,4,20]. The results of my measurements demonstrate that rotational distribution data provide a window on the partitioning of angular momentum between the photoelectron and ion. For single-photon ionization ($J_P = 1$), conservation of the angular momentum restricts $\Delta J = (l + 3/2), (l + 1/2), \ldots, -(l + 3/2)$ or $\Delta N = (l + 1), l, \ldots, -(l + 1)$, excluding electron spin [13]. The actual ΔN values that occur depend sensitively on microscopic aspects of the scattering dynamics, and the energy dependence in rotational distributions cannot be explained on the basis of atomiclike propensity rules [31]. However, the rotational distributions can be strongly influenced by the contribution of the angular momentum to the photoelectron matrix elements due to the torques exerted by the nonspherical molecular ion field [3,4,17,20]. Here, I present and discuss the results of rotationally resolved photoionization for the isoelectronic systems, N_2 and CO. The data obtained are tested for secondary processes, such as ionization induced by secondary photoelectrons, over a

range of stagnation pressures. Since the distribution of target states will vary with position in the molecular beam, I will also present evidence that the interaction region does not shift as the excitation energy is varied over a very wide range. These tests involve monitoring the beam spot using a phosphor screen employing sodium salicylate. I will show that these measurements are unambiguous and reproducible.

4.2 $N_2\ 2\sigma_u^{-1}$ Photoionization

The electronic configuration of the neutral N_2 target molecules is $1\sigma_g^2 1\sigma_u^2 2\sigma_g^2 2\sigma_u^2 1\pi_u^4 3\sigma_g^2$, and the term symbol is N_2 $(X^1\Sigma_g^+)$. In the excitation process, an electron is removed from the $2\sigma_u$ orbital, and we monitor fluorescence resulting from the radiative decay of a $3\sigma_g$ electron into the $2\sigma_u^{-1}$ hole. The rotationally resolved fluorescence spectra of N_2^+ are obtained for photon energies of $20 \le h\nu_{exc} \le 220$ eV by measuring the fluorescence intensities $I_{N^+N''}$ from the excitation and fluorescence sequence Eq.(4.1):

$$\begin{aligned} N_2\,(X^1\Sigma_g^+,\, v_0 = 0,\, N_0) + h\nu_{exc} &\rightarrow N_2^+\,(B^2\Sigma_u^+, v^+ = 0,\, N^+) + e^- \\ &\downarrow \\ &N_2^+\,(X^2\Sigma_g^+, v'' = 1,\, N'') + h\nu_{N^+N''}. \end{aligned} \tag{4.1}$$

Here v and N denote the vibrational and rotational angular momentum quantum numbers, respectively. The incident photon ionizes the neutral target molecules, with the photoelectron ejected from the $2\sigma_u$ orbital entering either the σ_g or π_g continuum channels. The rotational fluorescence intensities of the transition from the ionic excited state, N_2^+ ($B^2\Sigma_u^+$) (ionization potential 18.75 eV [44]), $v^+= 0$, N^+ to the ionic ground state, N_2^+ ($X^2\Sigma_g^+$), $v''= 1$, N'' are measured. Figure 4.1 shows typical N_2^+ rotationally resolved fluorescence spectra which are measured at photon energies of 40 eV and 192 eV. Since R–branch transitions ($\Delta N = N^+ - N'' = +1$) have greater rotational separations than those of the P–branch, they are better resolved in the R–branch, and this is where we will focus our attention whenever possible. By definition, it will be necessary to get information on the $N^+= 0$ level from the P–branch, since the lowest ionic rotational level in the R-branch is $N^+= 1$ (i.e., the R(0) line). It is clear from Fig. 4.1 that the relative intensities of the various transitions are dramatically different.

Since the fluorescence intensity $I_{N^+N''}$ of the rotational transition from N^+ to N'' is a measure of the population of rotational level N^+ (denoted as n_{N^+}), these spectra demonstrate that the photoion rotational distributions are changing dramatically.

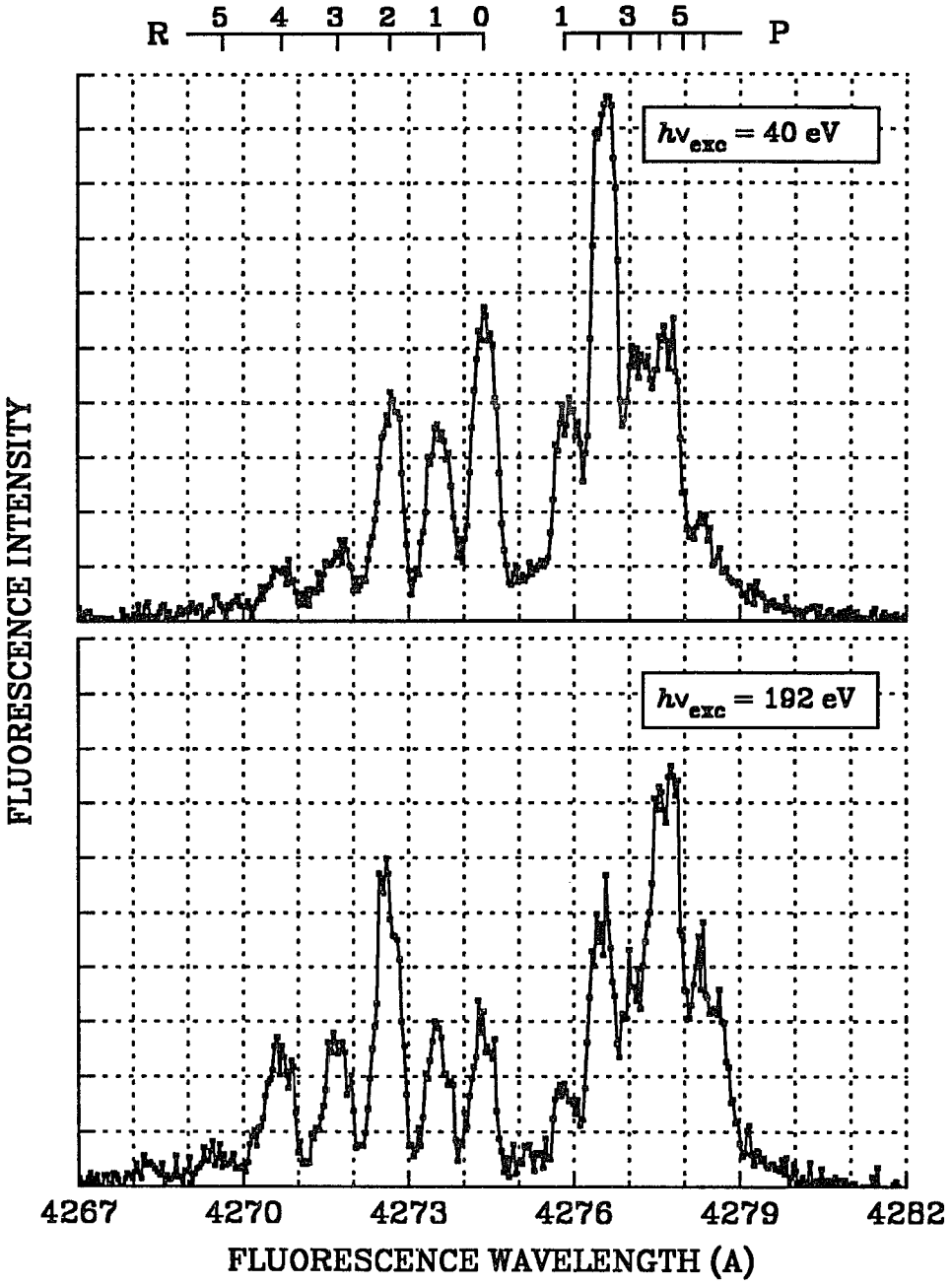

Fig. 4.1 Rotationally resolved fluorescence spectra $N_2^+(B^2\Sigma_u^+, v^+=0, N^+ \rightarrow X^2\Sigma_g^+, v''=1, N'')$ at excitation energies of 40 eV (top) and 192 eV (bottom).

To obtain the photoion rotational distribution, we determine the population n_{N^+} of each level from the relative fluorescence intensities. The relation between the observed intensities $I_{N^+N''}$ and the rotational populations n_{N^+} is given by Eq.(2.19). It can be rewritten as

$$n_{N^+} = K(2N^+ + 1)\,(I_{N^+N''}) / S_{N^+}, \qquad (4.2)$$

where K is a constant and S_{N^+} is a Hönl–London factor [37,48–50]. $S_{N^+} = N^+$ for R–branch transitions or $S_{N^+} = N^+ + 1$ for P–branch transitions. Using Eq.(4.2), the rotational populations up to the rotational level $N^+ = 5$ are determined from R–branch intensities while the population of the $N^+ = 0$ level is estimated from the P(1) transition. (The R(0) transition indicates the transition from the $N^+ = 1$ level.) The measured rotational populations of the ion are normalized (i.e., populations are reported as $(n_{N^+} / \Sigma n_{N^+})$ using rotational levels $N^+ = 0$–5, as the populations for $N^+ \geq 6$ are insignificant). Histogram plots of rotational distributions at 20 eV intervals are shown in Fig. 4.2. From this figure, one sees a large drop for $N^+ = 1$ and a 4-fold increase for $N^+ = 5$ as the photon energy increases from 30 to 210 eV. It provides clear evidence that the larger ΔN ionization transitions are becoming enhanced as the excitation energy is increased. It should be noted that the data in Fig. 4.2 are presented to identify the trends unambiguously

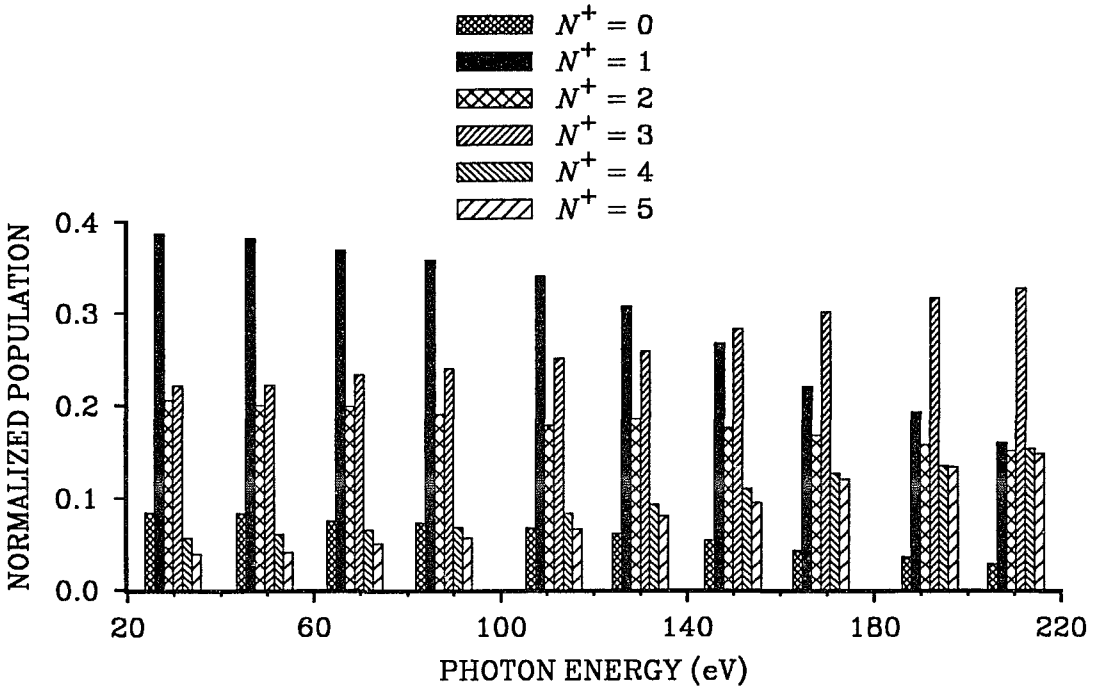

Fig. 4.2 Histogram plot of rotationally resolved ionic distributions for $N_2^+(B^2\Sigma_u^+)$ measured every 20 eV.

However, there are considerably more data than those shown in Fig. 4.2. In fact, fluorescence spectra were obtained at least every 5 eV. At lower energies, a denser energy mesh (typically 1 eV energy steps) is used. The complete data set for the populations ($n_{N^+}/\Sigma\, n_{N^+}$) are presented in Fig. 4.3 as a 3–D projection plot. For the $N^+ = 5$ level, the relative population increases by about a factor of four, while the population of the $N^+ = 1$ level falls by a factor of two.

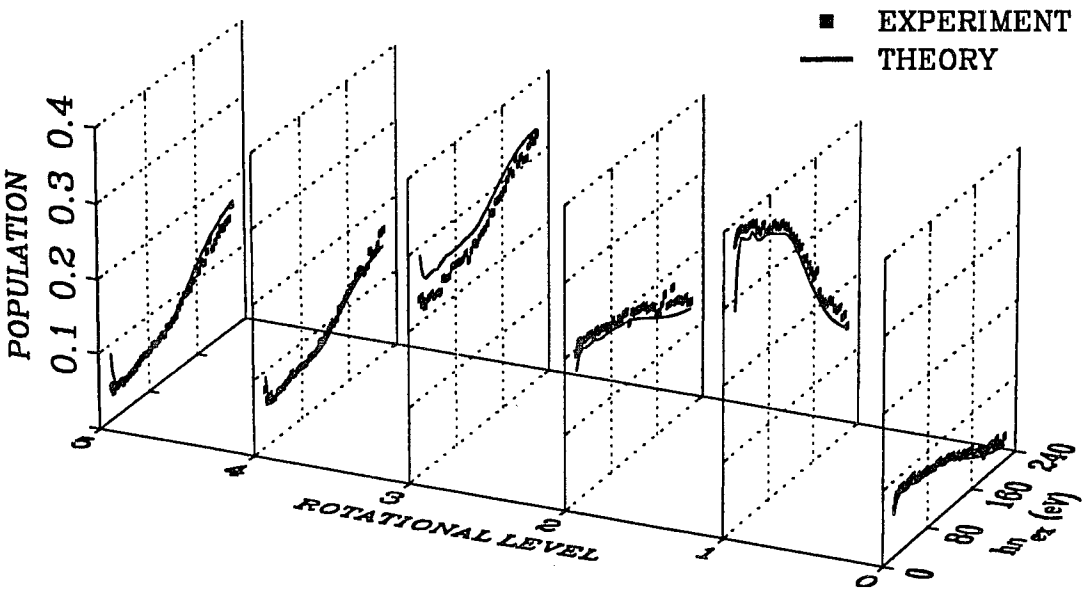

Fig. 4.3 Calculated (lines, reference [35]) and measured (dots) rotational photoion populations for $N_2^+(B^2\Sigma_u^+)$.

These results can be easily understood qualitatively if we assume that low ΔN transitions (i.e., $\Delta N = 1$) dominate at lower photon energies, while larger ΔN transitions (i.e., $\Delta N \geq 3$) grow in importance as the photon energy is increased. (Remember the selection rule that $\Delta N = \pm 1, \pm 3, \pm 5, \ldots$ owing to the inversion symmetry of N_2.). The rotational temperature of the target molecules is estimated to be 14 K, as will be shown in the following section.

4.3 Distribution Process in N_2 Photoionization

Since the population of each rotational level depends on the target rotational temperature, we need to examine the temperature of the target molecules. For the N_2 study, the initial temperature of target molecules is estimated as 14 K by Wang and McKoy [35] on the basis of experimentally obtained ionic rotational populations. To illustrate, theoretical ionic distributions at 3 different initial temperatures 10 K, 14 K and 18 K are shown with measured distributions in Fig. 4.4. It is obvious from Fig. 4.4 that agreement between calculated ionic distributions at 14 K and measurements is excellent over the spectra range. For our purposes, we will continue to estimate the target rotational temperature for $N_2(X^1\Sigma_g^+)$ to be 14 K.

There is another conclusion that we can extract from the comparisons shown in Fig. 4.4. Specifically, the qualitative trends are very similar for all three comparisons. There is comparatively little sensitivity of the comparison of theory and experiment on the initial temperature, and this will make the data analysis relatively simple as a result. Before describing the interpretation of the data in detail, it is useful to develop an overview of the distribution process. Assuming a target temperature of 14 K, the relative rotational populations of the target molecules (N_2) can be calculated using a Boltzmann distribution with the nuclear spin degeneracies.

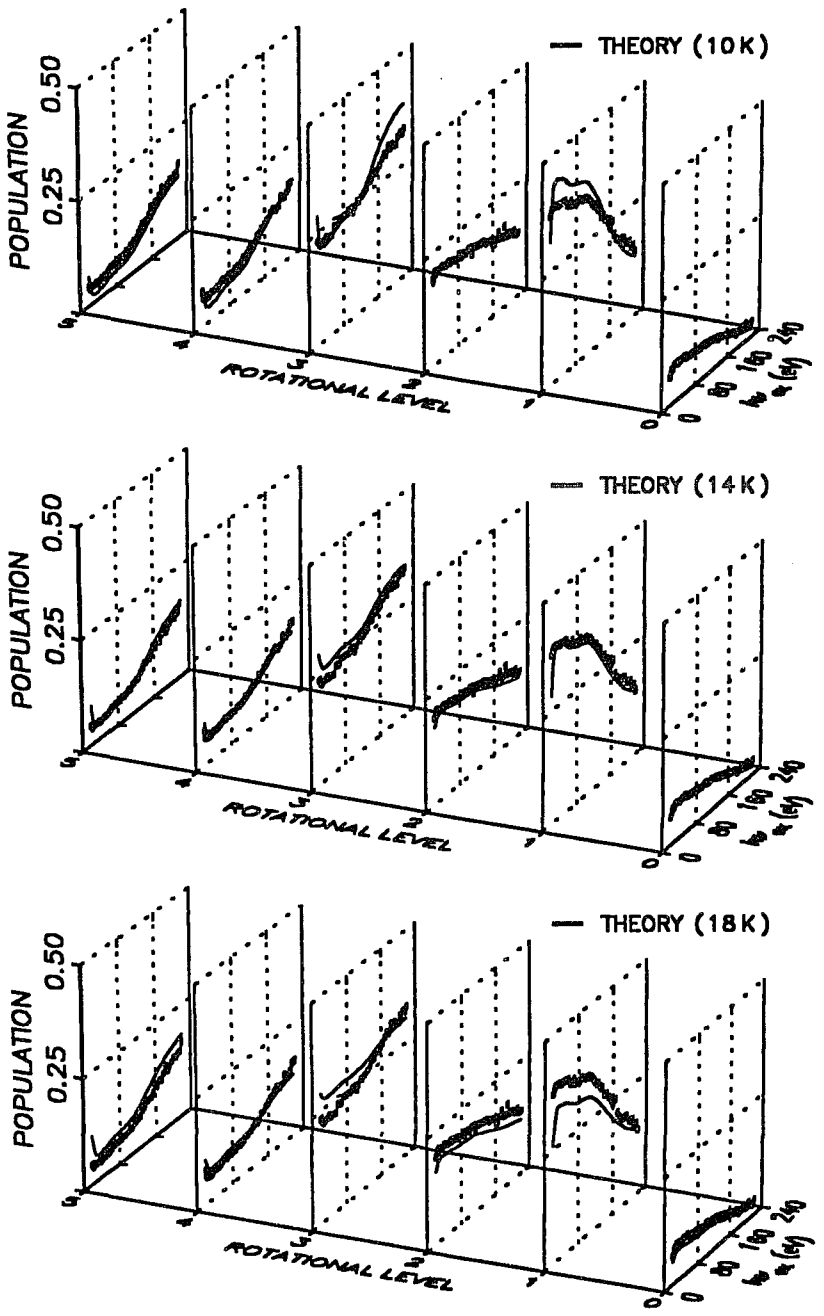

Fig. 4.4 Comparison of ionic populations between measurements and calculations at 3 different initial target temperature 10, 14 and 18 K. These calculations were done by Wang and McKoy.

As a result, the rotational populations for $N_{target} = 0–3$ are shown in Fig. 4.5. It is simple to show [48,50] that the only levels with appreciable populations are $N_{target} = 0, 1, 2$, while the populations of $N_{target} \geq 4$ are less than 5% and have an insignificant effect on the ionic distributions. If the dominant transitions are $\Delta N = \pm 1$ from this target distribution, one expects that the population of the $N^+ = 1$ level will be significant (~ 30 % of the total), while the $N^+ = 5$ level will be essentially unpopulated.

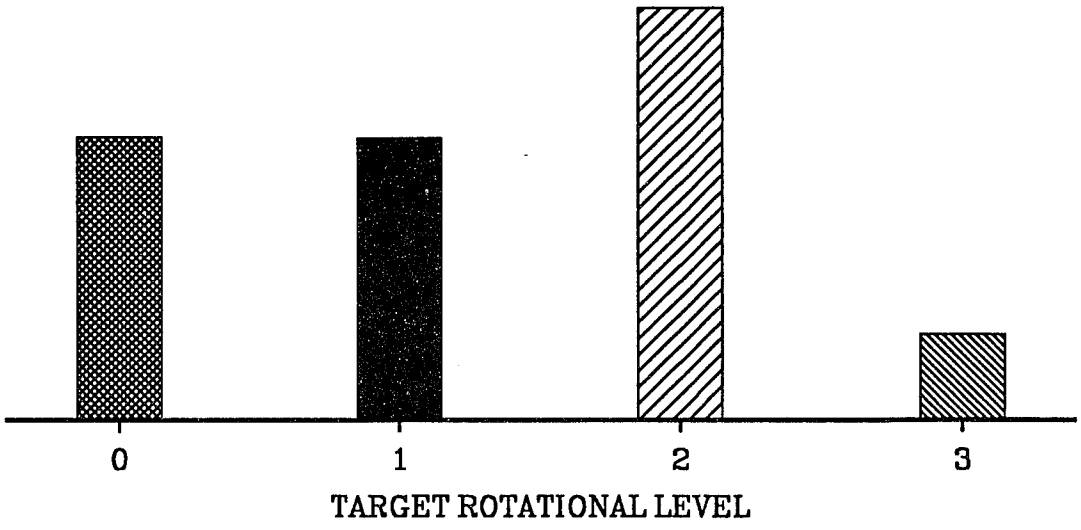

Fig. 4.5 Rotational thermal populations of target molecules N_2 at 14 K

However, as the $\Delta N = 3$ transitions increase with increasing energy [31,35], the $N_0 = 2 \rightarrow N^+ = 5$ transitions will begin to transfer appreciable population to the $N^+ = 5$ level. Similarly, the $N_0 = 0 \rightarrow N^+ = 3$ transitions will grow with increasing energy, which will deplete the $N^+ = 1$ level that was being populated by transitions out of the $N_0 = 0$ level at lower energies.

As a specific example of the photon energy 200 eV, the process of distributing populations from target to ionic rotational levels is illustrated step by step in Fig. 4.6. At this high photon energy, ionic populations resulting from specific target levels (in the middle diagram of Fig. 4.6) have $\Delta N = 3$ as well as $\Delta N = \pm 1$ transitions. The $\Delta N = 3$ transition from the target rotational level $N_0 = 2$ leads to appreciable population of the ionic rotational level $N^+ = 5$. Since the contribution to the resulting population of ionic rotational level $N^+ = 5$ is from target rotational level $N_0 = 0$ and 2, $\Delta N = 3$ and 5 transitions are possible. Of course, a $\Delta N = 1$ transition from $N_0 = 4$ could also populate the $N^+ = 5$, but this process is negligible due to the low population of $N_0 = 4$ level. The resulting (i.e., net) ionic populations shown in the top diagram of Fig. 4.6 indicate that ionic populations of $N^+ = 4$, 5 and 6 are gained due mainly to $\Delta N = 3$ transitions.

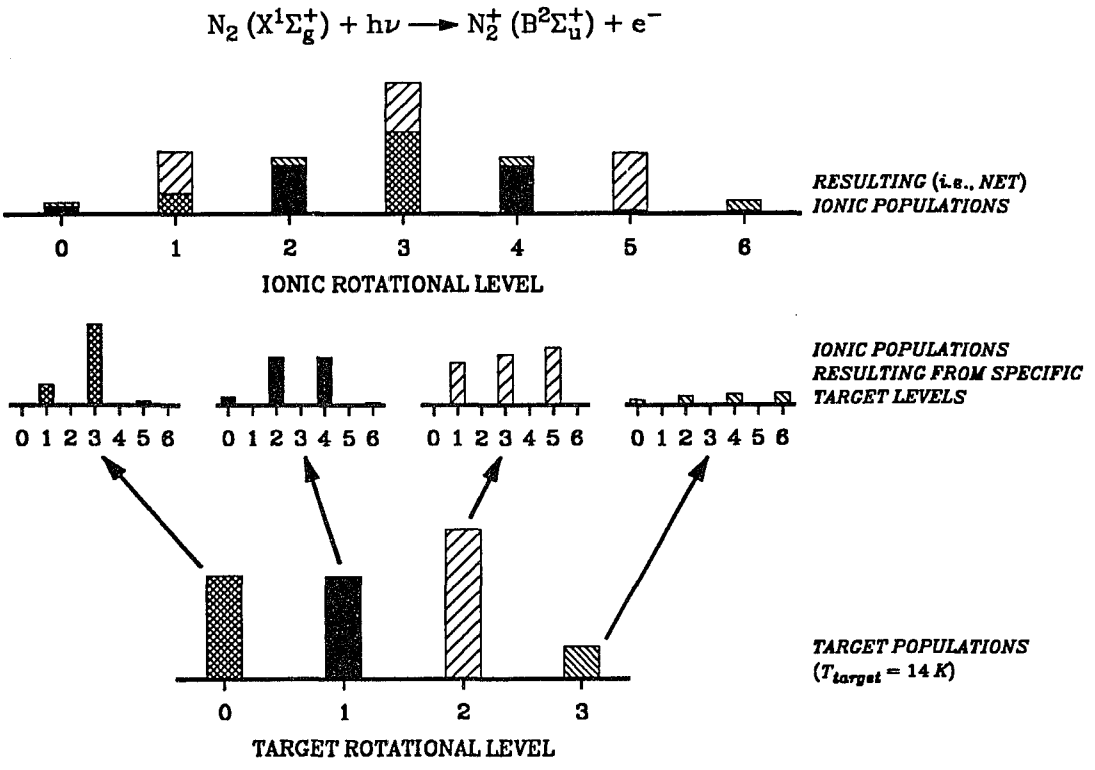

Fig. 4.6 Rotational excitation from the specific target rotational levels at high photon energy 200 eV.

Since the dependence of ionic populations on the ΔN as a function of the excitation energy is so critical, we need to examine what factors are related to it. These ideas can be quantified if it is possible to calculate the matrix elements and rotational transition strengths [35]. Fortunately, these experiments were followed by a series of calculations by Wang and McKoy [31,35].

4.4 Interpretation of Results

Now let us return to the comparison between experiment and theory shown in Fig. 4.3. There is good agreement between the calculated and the measured rotational distributions over the spectral range. It is instructive to take a closer look into the rotational distributions for the N^+= 1 and 5 levels, and this is given in Fig. 4.7.

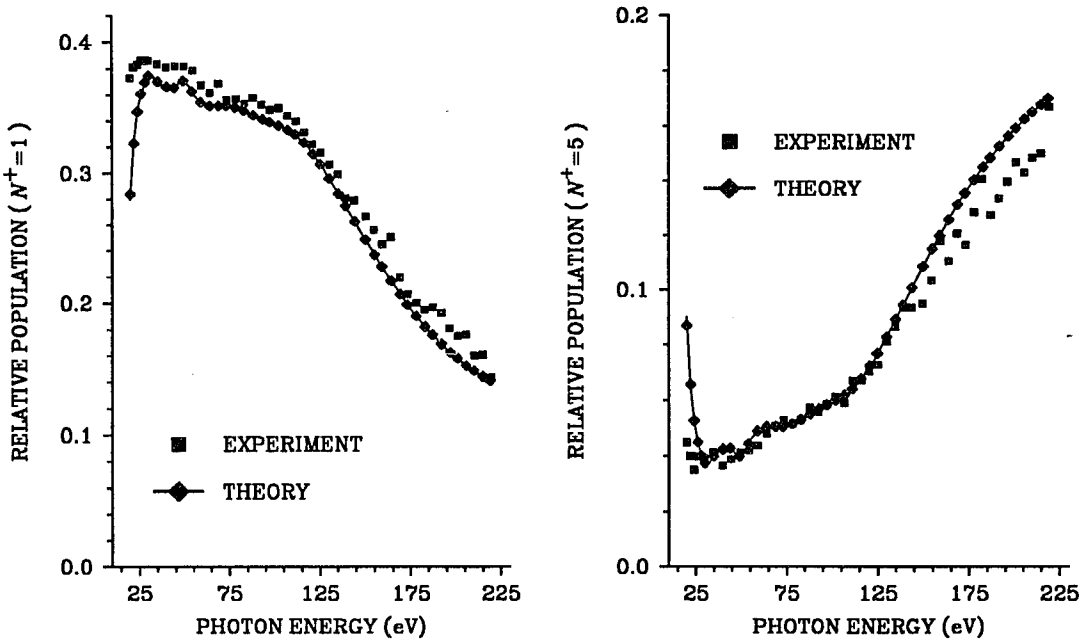

Fig. 4.7 Calculated and measured populations of N_2^+ for the strongly populated N^+ = 1 level (left) and the weakly populated N^+= 5 level (right) ; the diamonds on the line and the squares are data points from theoretical calculations (reference [35]) and from the measurements, respectively.

It is observed that there are essentially two regions in each of these plots, a region of slowly varying population below 120 eV and a region of quickly varying population above this energy. The inflection point is rather clear.

To gain insight into the causes of the inflection point at $h\nu_{exc} \approx 120$ eV, let us turn to the energy dependence of the dipole matrix element for the individual partial waves. The magnitudes of the partial wave components of the photoelectron matrix element $|D_l^{(-)}|$ were calculated by Wang and McKoy [35]. They are shown for the $2\sigma_u \rightarrow k\sigma_g$ and the $2\sigma_u \rightarrow k\pi_g$ channels in Fig. 4.8. (Note that $|D_l^{(-)}|$ is the magnitude of only one of the photon polarization indices μ in the molecular frame of the dipole matrix elements $\left|r_{fi}^{\Lambda\mu}\right|$ [17,35]). The selection rules dictate that $\Delta\Lambda = 0, \pm 1$ and $g \leftrightarrow u$ [37], so an electron in a $2\sigma_u$ orbital can leave in either the $2\sigma_u \rightarrow k\sigma_g$ or the $2\sigma_u \rightarrow k\pi_g$ continua. On the basis of the parity selection rule, $\Delta N + l =$ odd and inversion symmetry of N_2 [13,38], odd photoelectron partial waves are precluded. Finally, an $l = 0$ component is excluded in the $k\pi_g$ continuum due to the projection ($\Lambda = 1$), which exceeds the magnitude of the vector.

The analysis of the photoelectron matrix elements reveals that Cooper minima in the *d*-wave ($l = 2$) and the *g*-wave ($l = 4$) in the $k\sigma_g$ continuum occur at photon energies 140 eV and 100 eV, respectively [35].

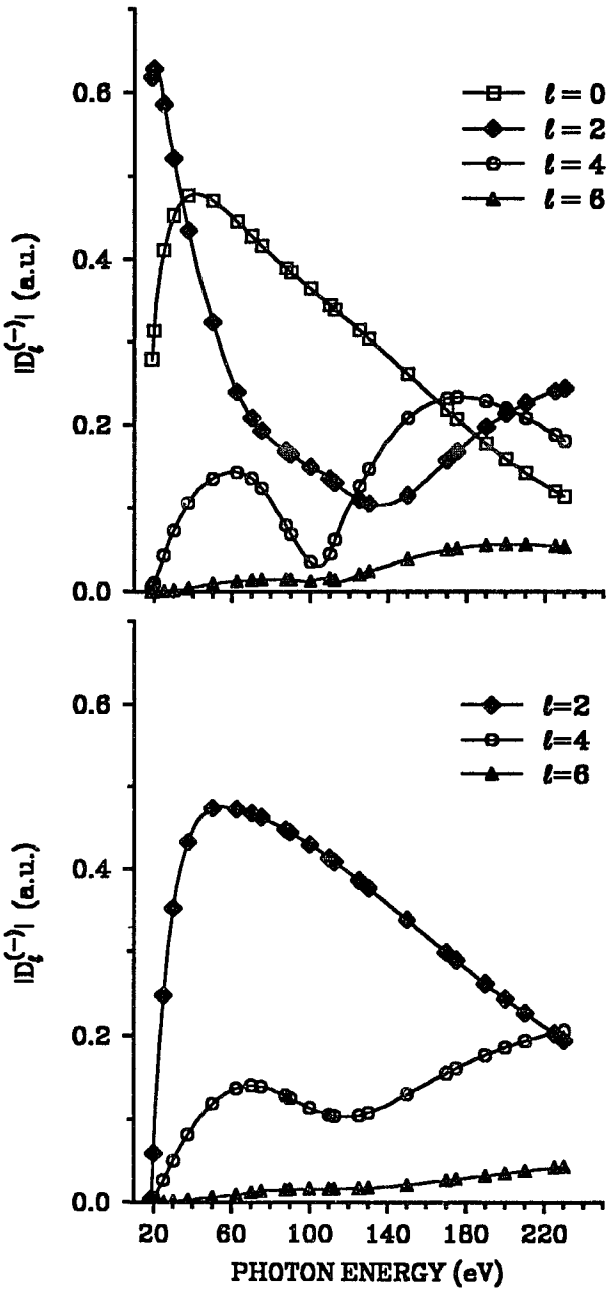

Fig. 4.8 Dipole strengths of partial wave components of the photoelectron matrix elements for the photoejection of the N_2 ground state in $2\sigma_u \rightarrow k\sigma_g$ (top) and $2\sigma_u \rightarrow k\pi_g$ (bottom) continuum channels from reference [35].

The formation of these Cooper minima depletes the contributions of the *d*- (l = 2) and *g*- (l = 4) waves at lower energies (i.e., ≤ 100 eV), allowing the *s*-wave (l = 0) to dominate in this region. This results in low ΔN transitions at low energy (i.e., $|\Delta N| = 1$). At higher photon energies ($h\nu_{exc}$ ≥ 150 eV), the magnitudes of the *g*-waves in the $k\sigma_g$ and $k\pi_g$ continua becomes comparable to that of the lower l components. These higher l contributions to the photoelectron matrix element lead to enhanced $\Delta N = 3$ transitions at higher photon energies. Since the $2\sigma_u$ orbital of N_2 ($X^1\Sigma_g^+$) has 90.7 % *p*-, 6.7 % *f*-, and 1.5 % *h*- (l_0 = 5) character [35], the high l contributions (like the *g*-wave) to the matrix element at high energies are not expected on the basis of an atomiclike propensity rule. However, ion rotational distributions are strongly influenced by off–diagonal distributions ($l \neq l'$) of the photoelectron matrix elements $r_{fi}^{\Lambda\mu}$ in Eq.(2.11), due to the nonspherical molecular ion potential [3,16,17].

4.5 CO $4\sigma^{-1}$ Photoionization

The electronic configuration of the neutral CO target molecules is $1\sigma^2 2\sigma^2 3\sigma^2 4\sigma^2 1\pi^4 5\sigma^2$. In our measurements, we eject an electron from the 4σ orbital, and detect the fluorescence as the 5σ electron relaxes to fill the $4\sigma^{-1}$ hole. In terms of the spectroscopic notation, we measured the

intensities of the rotationally resolved fluorescence described in Eq.(4.3). The ionization potential for creation of the CO^+ ($B^2\Sigma^+$) state is 19.7 eV [44]. Data were generated over the range 23 eV $\leq h\nu_{exc} \leq$ 140 eV. The excitation and fluorescence sequence for CO can be described as

$$CO(X^1\Sigma^+, v_0 = 0, N_0) + h\nu_{exc} \rightarrow CO^+(B^2\Sigma^+, v^+ = 0, N^+) + e^-$$

$$\downarrow$$

$$CO^+(X^2\Sigma^+, v'' = 1, N'') + h\nu_{N^+N''}. \quad (4.3)$$

Note that this sequence is isoelectronic with the N_2 process described earlier. Our initial expectations were that the two systems would be similar in their qualitative behavior.

By measuring the intensities $I_{N^+N''}$, we obtain the rotational fluorescence spectra for CO^+, and Fig. 4.9 shows a typical spectrum at photon energy of 35 eV. Also shown as a solid line in Fig. 4.9 is the result of a gaussian–fitting procedure to extract the relative intensities. The conditions of the optical system for CO are the same as those for N_2 except for the reduced slitwidth (80 μm) of the fluorescence monochromator. The resolution requirements for CO^+ are more demanding than those for N_2^+. For example, the separation between the P(1) and P(2) transitions is less than 0.3 Å. Fluorescence spectra for CO^+ are obtained at least every 10 eV. At lower energies, measurements are every 1 eV.

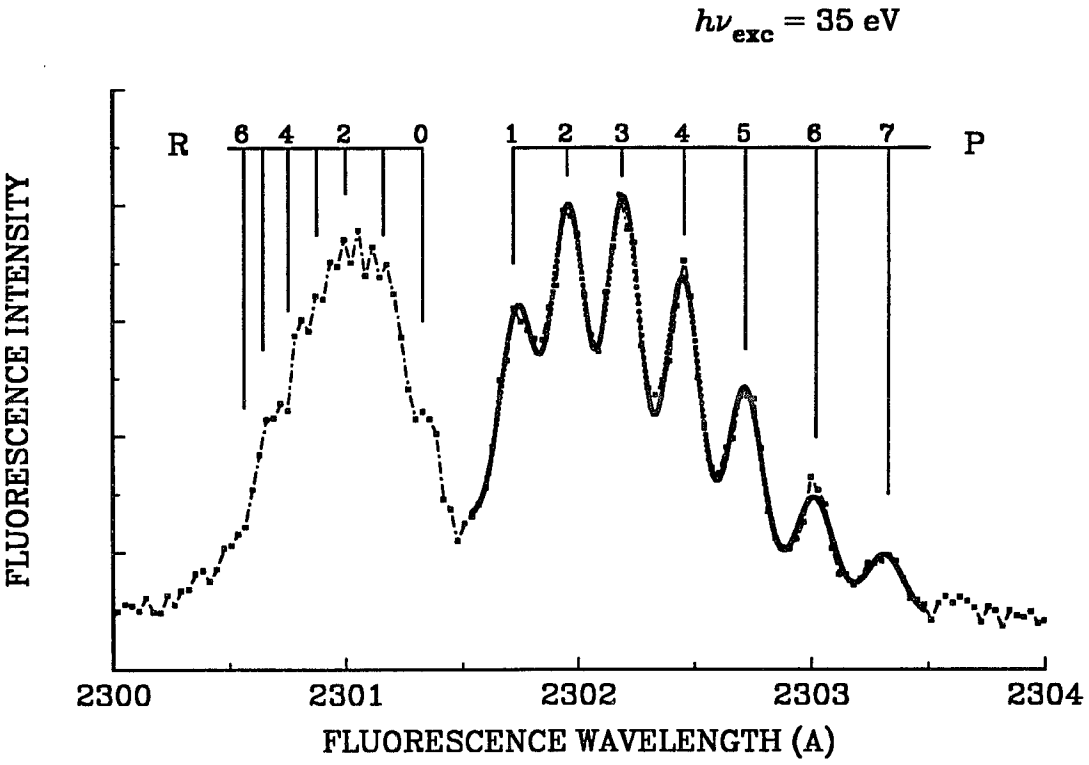

Fig. 4.9 Rotationally resolved spectra of CO^+ ($B^2\Sigma^+$,v^+= 0, $N^+ \rightarrow X^2\Sigma^+$, v''= 1, N'') at $h\nu_{exc}$= 35 eV.

The theoretical calculations and experimental measurements for the normalized populations ($n_{N^+}/\Sigma n_{N^+}$) are plotted as a function of the photon energy in Fig. 4.10. The experimentally determined relative populations are determined from the P–branch transitions, and are shown in Fig. 4.10. The calculated distribution is also shown [35].

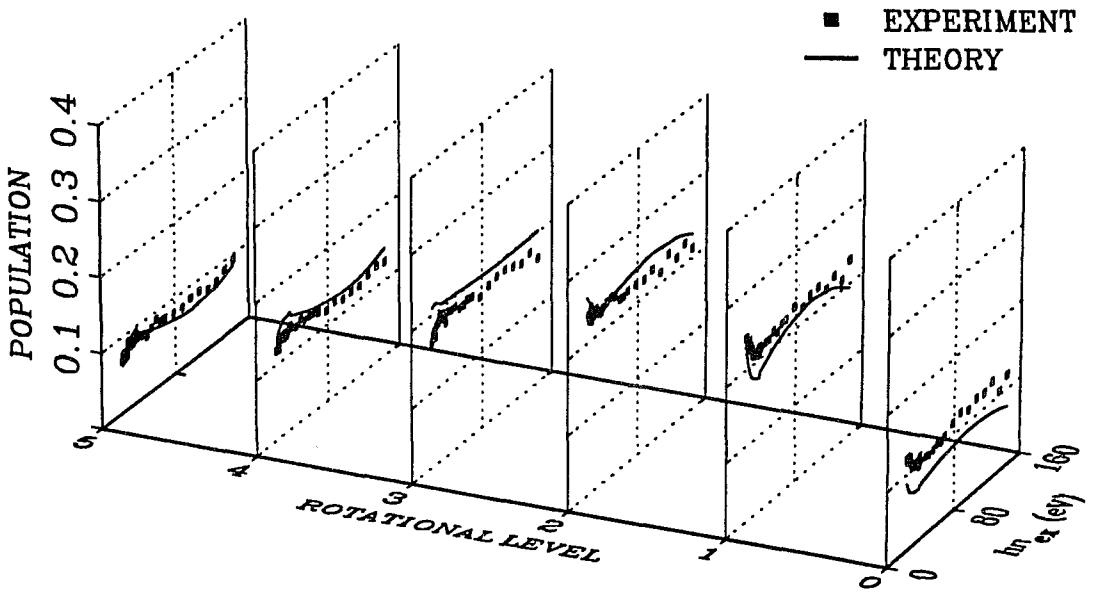

Fig. 4.10 Calculated (solid lines, reference [35]) and measured (dots) rotationally resolved photoion distributions for $CO^+(B^2\Sigma^+)$ over the excitation photon energy of $23 \leq h\nu_{exc} \leq 145$ eV.

The calculations assumed the temperature of the neutral ground state CO ($X^1\Sigma^+$) to be 18 K, and the agreement between experiment and theory is good, although not as striking as the agreement for the N_2 results. In contrast to the large changes in the rotational distributions for N_2^+ ($B^2\Sigma_u^+$), populations of all rotational levels for CO^+ ($B^2\Sigma^+$) remain comparatively flat over the whole spectral range, showing little dependence on the photon

energy. Small features in both the measured and calculated rotational distributions occur at $h\nu_{exc} \approx 37$ eV. This is ascribed to an *f*-wave shape resonance [42,56]. Although the apparent influence on the rotational distributions appears to be minor, a detailed inspection of calculated results will reveal otherwise.

By applying the electronic selection rule $\Delta\Lambda = 0, \pm 1$ [37], it can be shown that the electron ejected from the 4σ orbital can exit via the $4\sigma \rightarrow k\sigma$ and $4\sigma \rightarrow k\pi$ ionization channels. On the basis of the parity selection rule for a $\Sigma^+ - \Sigma^+$ transition, both even and odd ΔN transitions are allowed [13,38], in contrast to N_2. The magnitudes of dipole strengths of the partial wave matrix elements for CO are calculated as a function of the photon energy [35], and plotted for $4\sigma \rightarrow k\sigma$ and $4\sigma \rightarrow k\pi$ ionization channels in Fig. 4.11. Again, the $l = 0$ component is excluded from the $k\pi$ ionization channel (i.e., $\Lambda = 1$), as the projection of an $l = 0$ function cannot equal 1. Figure 4.11 shows an *f*-wave shape resonance peaking at kinetic energy ~19 eV (photon energy ~38.7 eV) in the $k\sigma$ continuum and an *f*-wave broad enhancement in the $k\pi$ continuum peaking at kinetic energy ~30 eV. The contributions of strong $l = 3$ components in both the $k\sigma$ and $k\pi$ continua lead to large ΔN transitions at low photon energy while the other high l components of the photoelectron support this trend at the high photon energy, leading to large ΔN transitions.

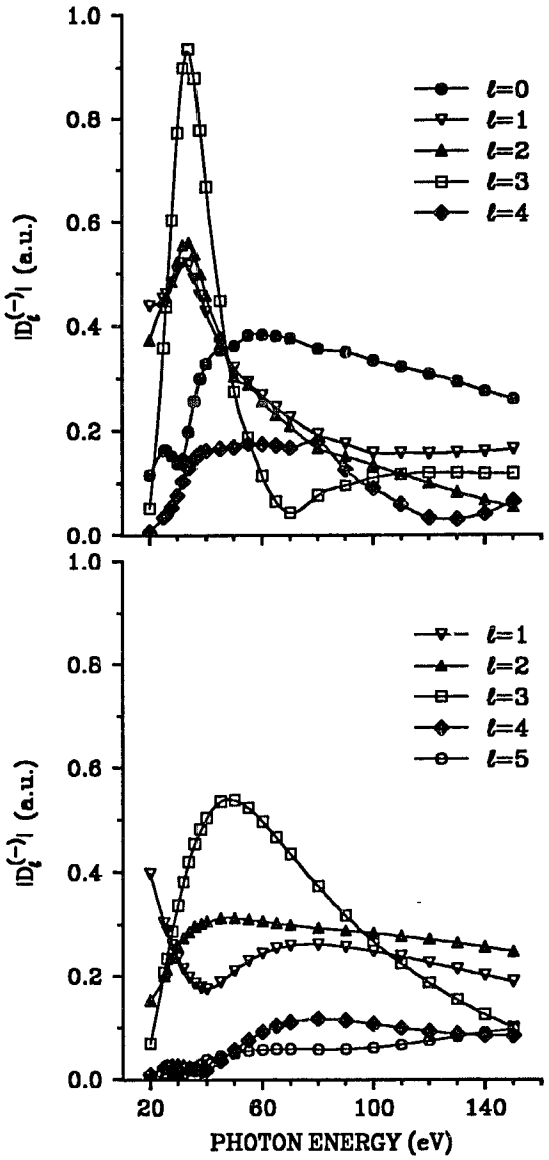

Fig. 4.11 Dipole strengths of partial wave components of the photoelectron matrix elements for the photoejection of the CO ground state in $4\sigma^{-1} \rightarrow k\sigma$ (top) and $4\sigma^{-1} \rightarrow k\pi$ (bottom) continuum channels from reference [35].

These large contributions of high l components to the photoelectron matrix elements over the whole spectral range are responsible for the comparatively flat behavior in the rotational distributions seen in Fig. 4.11.

4.6 Direct Comparisons between N_2 and CO

The previous sections describe the rotationally resolved fluorescence results for the isoelectronic systems N_2 and CO over an extended energy range. At this juncture, it is useful to compare the two data sets in greater detail. In Fig. 4.12, we compare the populations of the rotational $N^+ = 1$ level for N_2^+ and CO^+. As a result, the difference in the ion rotational distributions for the isoelectronic system reveals a strikingly unusual and different energy dependence.

For N_2, the analysis of the photoelectron matrix elements reveals that Cooper minima occur in the d-wave ($l = 2$) at the photon energy 140 eV and in the g-wave ($l = 4$) at the photon energy 100 eV of the $k\sigma_g$ continuum state [35]. Since the formation of these Cooper minima depletes the d- ($l = 2$) and g- ($l = 4$) continuum waves, the low s-wave ($l = 0$) in the $k\sigma_g$ continuum state dominates, resulting in low ΔN transition at the range of these photon energies.

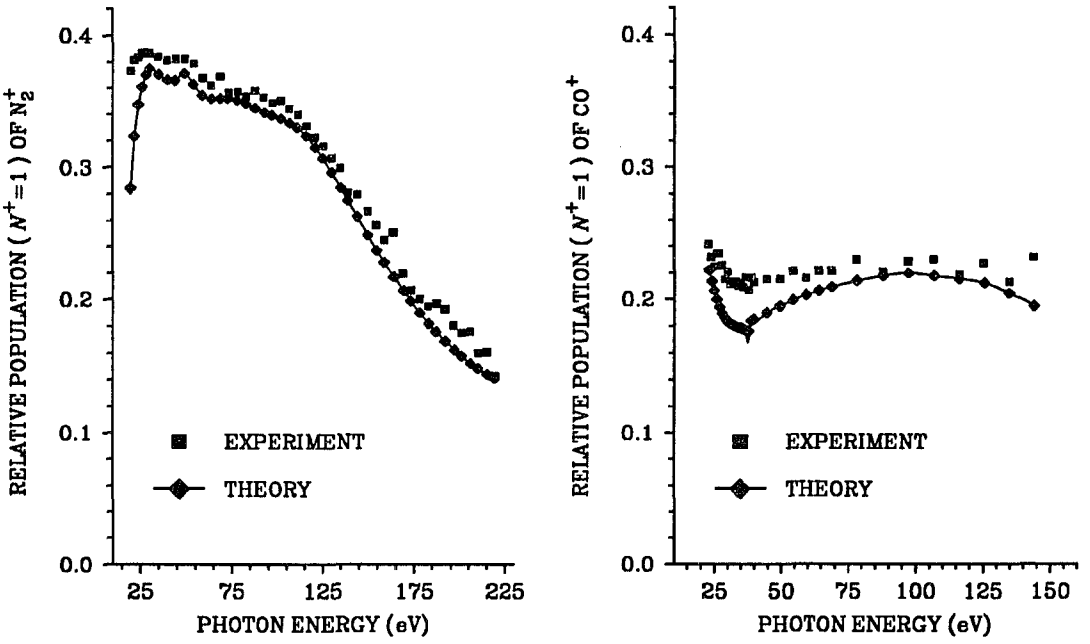

Fig. 4.12 Calculated and measured relative populations of the strongly populated $N^+ = 1$ level for the N_2^+ state (left) and the CO^+ state (right).

At high photon energies ($h\nu_{exc} \geq 170$ eV), on the other hand, the magnitude of *g*-waves ($l = 4$) in the $k\sigma_g$ and $k\pi_g$ continua is comparable to the magnitudes of the *s*-wave ($l = 0$) and *d*-wave ($l = 2$). The high l component of the photoelectron matrix elements consequently leads to large ΔN transitions. In the evaluation of dipole matrix elements $r_{fi}^{l\lambda\mu}$, off–diagonal terms ($l \neq l'$) arise in Eq.(2.11) due to the nonspherical molecular field during the escape

[17]. Thus, the coupling of angular momentum between partial waves l and l' can be viewed as arising from torques exerted on the outgoing electron by the interaction of the nonspherical molecular field [3,4,17,20], and this angular momentum coupling makes a photoelectron orbital an admixture of angular momentum components [17]. This unusual behavior cannot be explained on the basis of an atomiclike propensity rule for the photoionization of the $2\sigma_u$ orbital of the $X^1\Sigma_g^+$ ground state with its 90.7 % *p*-, 6.7 % *f*-, and 1.5 % *h*- ($l_0 = 5$) character [35]. This change from smaller to larger ΔN transitions due to the Cooper minima and the contributions of the higher l components provides an explanation of the trend observed in photoion rotational distributions for N_2. Results of analogous measurements of ion rotational distributions for CO are shown in Fig. 4.10. Unlike the N_2 results, the rotational distributions of CO^+ show essentially no dependence on the excitation energies. A comparatively small feature in the rotational distributions at $h\nu_{exc} \approx 37$ eV are interpreted as being due to an *f*-wave shape resonance for the direct ejection of the 4σ electron of CO [54]. It is notable that the *f*-wave shape resonance is not observed in the $2\sigma_u^{-1}$ photoionization of N_2 owing to its symmetry [13,31,38]. The magnitudes of the partial wave components of the photoelectron matrix element $|D_l^{(-)}|$ are calculated as a function of the photon energy and shown in Fig. 4.11. For the photoionization of CO, the 4σ orbital in the $X^1\Sigma^+$ ground state is allowed to make a

transition in kσ and kπ continuum states, where its transition is governed by the selection rule of electronic transition $\Delta\Lambda = 0, \pm 1$ [13,37,38]. All ΔN transitions are allowed on the basis of the parity selection rule of $\Sigma^+ - \Sigma^+$ transition [13,38] for the photoionization of CO, and $l = 0$ (s-wave) component of photoelectron in the kπ continuum channel is exempt due to the projection of the π channel ($\Lambda = 1$). The analysis of the photoelectron matrix elements $r_{fi}^{l\lambda\mu}$ for CO^+ predicts an f-wave shape resonance peaking at kinetic energy ~19 eV in the kσ continuum state and a broad enhancement of the f-wave ($l = 3$) component peaking at kinetic energy ~30 eV in the kπ continuum state. The contribution of the strong f-wave ($l = 3$) component in the kσ and kπ continuum states to the photoelectron matrix element lead to large ΔN transitions at the low photon energy range [35]. And the other higher l components of partial waves support large contributions to the matrix element at high photon energy, leading to large ΔN transitions. Therefore, the f-wave shape resonance in the kσ channel and the broad enhancement of the f-wave in the kπ are responsible for the flat behavior in the rotational distribution that is shown in Fig. 4.11. Since the 4σ orbital in the $X^1\Sigma^+$ ground state of CO has 14.6 % s-, 62.3 % p-, 15.7 % d-, 3.1 % f-, and 2.7 % g- ($l_0 = 4$) character [35], dominant contributions of s- and d-waves to the photoelectron matrix element are expected on the basis of the atomiclike propensity rule.

However, these *f*-wave enhancements are molecular in origin and are due to the torques exerted by the nonspherical molecular ion field [31].

Instead of simply reporting the populations of individual levels, as has been done for all of the previous discussion, it can be useful to present the data in a somewhat more compact form. Specifically, the rotational populations can be fitted to a Boltzmann distribution to determine an effective ionic temperature. Clearly, this is just a parameterization of the data, as we are not dealing with a system at thermal equilibrium. However, it is a useful parameterization, as will be shown below. The rotational level populations are determined from the relative fluorescence intensities using Eq.(4.2), as was done before. The simple relation between the rotational distribution obtained from Eq.(4.2) and the Boltzmann distribution Eq.(2.14) is given as

$$(2N^{+}+1)\cdot\frac{I_{N^{+}N''}}{Kd_{I}S_{N^{+}}}=C\cdot(2N^{+}+1)\cdot\exp\{-B_{v^{+}}N^{+}(N^{+}+1)/\tilde{k}T\}. \qquad (4.4)$$

Since the homonuclear molecular N_2 has alternating intensities with a ratio of 2 : 1 due to the total degeneracies of the rotational levels [37], rotational distributions need to be normalized for the nuclear spin degeneracy. For the case of $^{14}N_2$ (nuclear spin $I = 1$), the nuclear spin degeneracies $d_I = 2$ for odd N^+ levels and $d_I = 1$ for even N^+ levels are used for normalization [50]. In Eq.(4.4), $B_{V}+$ is the v^+–dependent rotational constant, and is estimated as

2.0733 cm^{-1} for N_2^+ ($B^2\Sigma_u^+$, $v^+= 0$) [37]. From Eq.(4.4), we can determine the ionic rotational temperature T by plotting a least squares fitting of $\ln[K I_{N^+N''}/(d_J S_{N^+})]$ versus N^+ ($N^+ + 1$). By repeating this procedure at many excitation energies, we can obtain a temperature vs. energy plot, such as that shown in in Fig. 4.13.

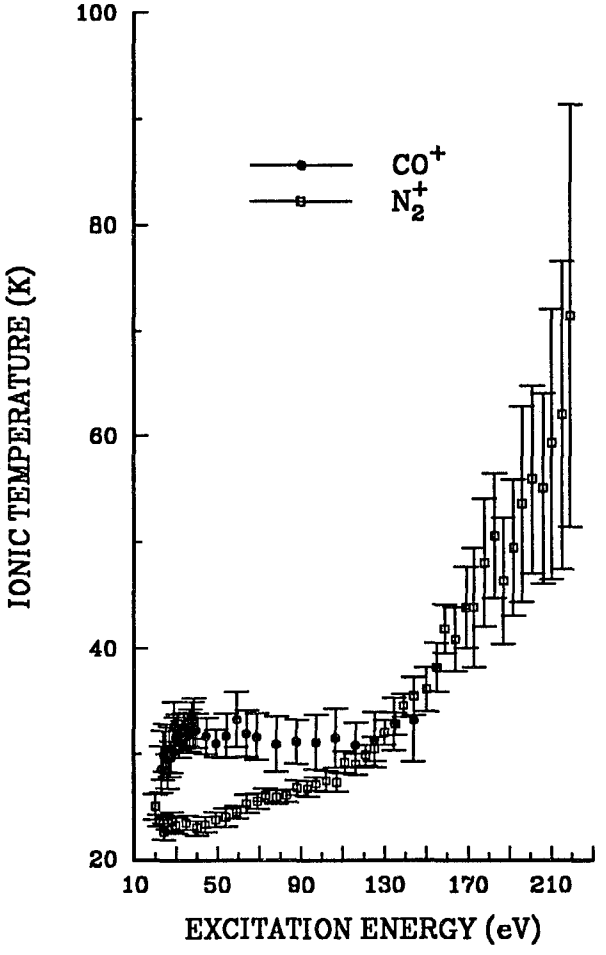

Fig. 4.13 N_2^+ and CO^+ photoion rotational temperatures (statistical errors).

For the calculation of the rotational temperatures, a Boltzmann function for the distribution of $N^+ \geq 1$ is assumed. This fits the data quite well at the lower photon energies, but the quality of the fit is poor at higher energies, and this poor fitting is the reason for the large error bars at higher energy, not poor data quality. It is clear that the data shown in Fig. 4.13 graphically illustrate the dramatic differences in the photoionization dynamics for the N_2 and CO systems. Moreover, this is a very compact representation of the overall trends. The present N_2^+ ($B^2\Sigma_u^+$) rotational temperature results show quite different behavior from the electron-impact ionization studies which were alluded to earlier. While the electron-impact studies show almost no dependence of the N_2^+ ($B^2\Sigma_u^+$) rotational temperature on the electron scattering energy [50], the present photoionization results show dramatically increasing rotational temperatures. This indicates that the simplified excitation models employed previously [48,49] may be of limited use, as the ionization dynamics show that the electronic motion and the nuclear motion can vary strongly with the electron kinetic energy.

4.7 Pressure–dependent Tests for Secondary Processes

When the data taking was in progress, the question arose as to whether the large changes in the N_2 rotational distributions were due to changes in the

ionization dynamics or unwanted effects in the measurements, such as secondary scattering processes. For example, it was considered that as the photon energy was increased, the photoelectrons produced would have increasing energy, and might create additional excited state ions by electron-impact ionization. As the electron scattering energy would be increasing, so might the rotational distributions of the "secondary" ions. As a result, it might be possible that the effects that I observed could be due to some process essentially independent of the one that was the focus of the study.

It was necessary to test for such secondary processes, but there were problems with developing such tests. The typical way that one might test for pressure dependent effects is to vary the pressure of the sample and see if the results change. Unfortunately, varying the pressure of the sample means that one must also vary the rotational temperature of the target molecules. This will change the relative ionic populations even if no secondary artifacts are corrupting the data. This pressure dependent problem complicates the test for artifacts considerably. In order to test for secondary processes, I did in fact proceed by varying the sample pressure. It was the data presentation that allows us to correct for the changing rotational temperature of the target molecules. To search for secondary processes, we obtained rotationally resolved fluorescence data sets for N_2 at different chamber pressures, specifically $P_{ch} = 2.0\times10^{-4}$, 5.6×10^{-4}, and 8.0×10^{-4} Torr, by adjusting

stagnation pressures behind the aperture to $P_S = 80$, 170, and 280 psig, respectively. These data were analyzed using the rotational temperature parameterization employed above, and the results are shown in Fig. 4.13. Since higher stagnation pressure results in greater rotational cooling, the ionic temperature is expected to increase as the stagnation pressure is decreased. In fact, the data sets for lower pressures $P = 5.6\times10^{-4}$ and 2×10^{-4} Torr exhibit increased ionic temperatures compared to the data set for $P = 8\times10^{-4}$ Torr.

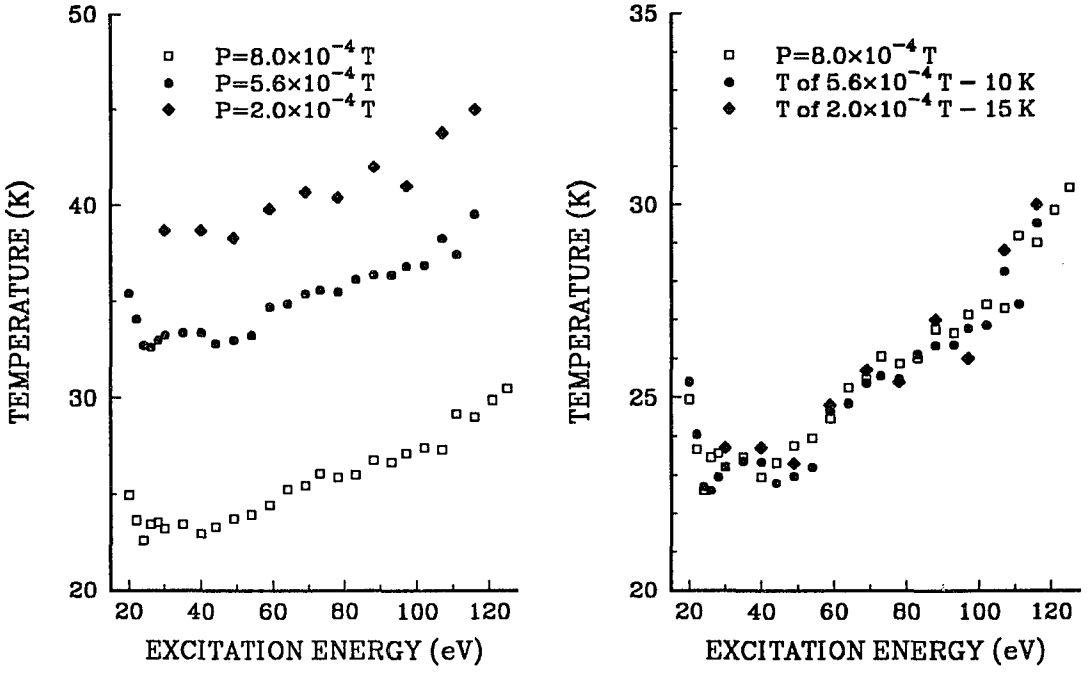

Fig. 4.14 Left frame: unaltered energy dependence of ionic rotational temperatures for N_2^+ ($B^2\Sigma_u^+$) at 3 different pressures. Right frame: data sets for $P = 5.6\times10^{-4}$ and 2×10^{-4} Torr are lowered 10 and 15 K, respectively.

In the right-hand frame of Fig. 4.14, the data are adjusted in an illuminating way. The ionic temperatures for the lower pressure P = 5.6×10^{-4} and 2×10^{-4} Torr are shifted to the data set for P = 8×10^{-4} Torr by lowering 10 K and 15 K, respectively. All data sets overlap well, and demonstrate the same trend as a function of photon energy over the entire range studied. This is a clear indication that the rotational excitation in ionization behaves similarly for all three pressures studied, indicating that the trends observed reflect the primary ionization process and not unwanted secondary effects. Of course, the excellent agreement between experiment and theory gives additional credence to the claim that the experiment is measuring a primary process, but these experimental data give us additional confidence in the results.

There is an added benefit to this parameterization of the data, although it should not be taken too far. Specifically, it is a very compact way of representing the data, as all the rotational populations for a given photon energy (n_{N^+} = 1–5 specifically [50]) are represented by a single value, i.e., the apparent rotational temperature. This gives us another opportunity to compare the qualitative behavior of N_2 and CO, which is done below. This comparison serves to reinforce the earlier contention that the qualitative behaviors of N_2 and CO are really quite different.

4.8 Tests for Beam Motion Effects

As the first user of the plane grating monochromator (PGM) beam line, it is necessary to test for artifacts that might be induced by motion of the incident VUV photon beam. We are able to see the beam position in the chamber using a sodium salicylate mounted on a linear motion feedthrough. As excitation energies are combined 30, 100, and 200 eV, the beam position and spot size on the phosphor screen do not change appreciably, and we place an upper limit of any motion at 0.5 mm. A few data points are obtained for different gas jet positions. For example, when we change the X position of the gas jet by 3 mm from the original position (X = −0.1") to X = 0.05", the count rate drops 20 % and the ionic temperatures increase ~5 K with the same trend as shown in Fig. 4.15. It indicates that the temperature changes are really very slight given the comparatively large shifts of the gas jet. The main point of this demonstration is that the motion of the beam, or slight shifts in the interaction volume due to experimental instabilities, could not be responsible for the huge temperature changes observed in the experimental data shown in Fig. 4.13 and previous sections. The changes observed in the N_2^+ ($B^2\Sigma_u^+$) distributions are apparently due to the nascent photoion distributions and not to unwanted artifacts.

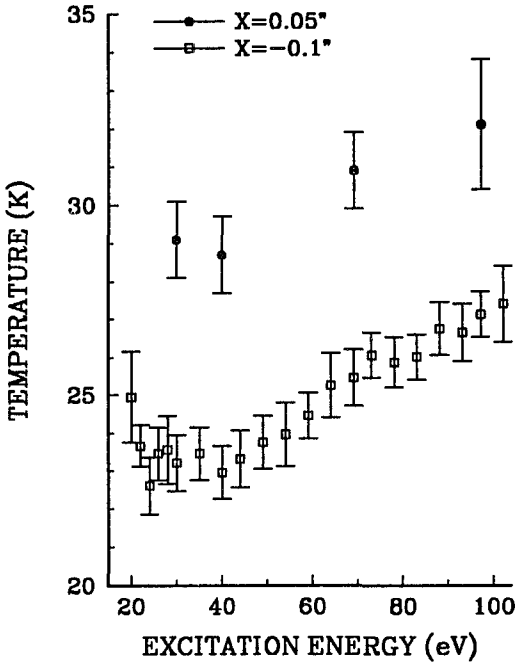

Fig. 4.15 Effect of gas jet position on N_2^+ ($B^2\Sigma_u^+$) rotational temperatures.

4.9 Measurements of Beam Line Parameters

Additionally, we estimate bandwidths of excitation energies for the fully opened entrance and exit slits at 5 different premirror angles, i.e., 77.1°, 77.5°, 80°, 82° and 85°. Since the Al filter has a sharp cut–off at ~70 eV [55], we measure its cut–off width of between start and end point by scanning in 0.1 eV energy steps. We estimate the excitation energy bandwidth as 80 % of the measured Al filter cut–off width due to its uncertainty. The averaged

bandwidths are tabulated according to angles of the premirror corresponding to the photon energy ranges used in Table 4.1. Since the fluorescence detection bandwidth is not related to or limited by the excitation bandwidth, the study of highly resolved photoionization is feasible regardless of the excitation bandwidth. These data are useful for general information in the planning of other experiments which may be dependent on the excitation bandwidth.

Operating Energy Range	Premirror Angle	Excitation Bandwidth
$20 \leq h\nu_{exc} \leq 30$ eV	77.1°	1.03 eV
$30 \leq h\nu_{exc} \leq 80$ eV	77.5°	0.95 eV
$80 \leq h\nu_{exc} \leq 100$ eV	80°	0.75 eV
$100 \leq h\nu_{exc} \leq 150$ eV	82°	0.65 eV
$150 \leq h\nu_{exc} \leq 220$ eV	85°	0.5 eV

Table 4.1 Measured excitation bandwidths of PGM beam with fully opened entrance and exit slits at 5 premirror angles.

For example, some resonant phenomena (e.g., autoionization) are considerably narrower than the features studied in my work, and knowledge of the incident bandwidth is critical in such circumstances.

CHAPTER V.

CONCLUSION

We obtain highly resolved dispersed fluorescence spectra for the isoelectronic systems, N_2 and CO, over an extended energy range using synchrotron radiation from the LSU CAMD–PGM. The primary motivation for this study is to probe the partial wave composition of the outgoing photoelectron and the partitioning of the angular momentum between ion and electron by monitoring ionic rotational distributions over a broad range of the excitation energy.

Numerous rotational studies have shown that the change in the rotational angular momentum ΔN can provide valuable propensity rules in molecular photoionization [11–13,22–24]. Also, rotationally resolved data yield significant insights into fundamental scattering dynamics, providing a window on the partitioning of angular momentum between photoelectron and ion core. In the earlier study [27], an example of a rotational branching ratio I[R(4)] / I[band] for N_2 photoionization is obtained as a function of the excitation wavelength near the threshold, showing a distinct dip at λ_{exc} = 550 A. Owing to the observed resonance dip, dipole selection rules cannot be assumed to govern the angular momentum deposition for the ion. Instead, dipole selection rules constrain the total angular momentum of the ion–

photoelectron complex, while the angular momentum partitioning between ion and electron depends on the photoejection dynamics [27]. By extending the spectra range, my study has more completely elucidated the photoelectron ejection dynamics. My study also provides much more detailed information by determining rotational populations for all the rotational levels. This reflects the better instrumental capabilities for the current studies. Both the increased sensitivity and broader range aspects of the current study are made possible by the 6 meter PGM at CAMD, and this work serves as the first data set from synchrotron radiation of the LSU CAMD–PGM.

The measured results show a remarkably unusual and different energy dependence, although a different dependence is expected due to absence of a center of symmetry in CO. The calculated spectra for N_2 and CO show generally good agreement with the experimental results in the rotational distributions. Moreover, the unexpected behavior is explained in terms of the photoelectron matrix elements. I summarize the principal conclusions from the measurements and calculations.

1. For the photoionization of N_2^+ $(2\sigma_u^{-1})$,

   - Cooper minima of *d*- and *g*-waves allow to dominate the *s*-wave contribution to the photoelectron dipole matrix element at the low photon energy, leading to low ΔN transitions.

- The magnitude of *g*-waves in continuum channels is comparable to the *s*- and *d*- waves, resulting in large ΔN transitions.
- Thus, the ion rotational distribution shows dramatic changes as a function of the excitation energy.

2. For the photoionization of $CO^+(4\sigma^{-1})$,

- The *f*-shape resonance and the *f*-wave enhancement in the $k\sigma$ and $k\pi$ continuum channels dominate at the low photon energy, leading to large ΔN transitions.
- The other high partial waves sustain large contributions to the dipole matrix element at the high photon energy, resulting large ΔN transitions.
- Therefore, the ion rotational distribution tends to be flat as a function of the excitation energy.

Listed below are conclusions relevant to instrumental issues, which might be useful in planning future activities.

3. For dispersed fluorescence detection following photoionization,

- The present results use a high resolution probe of photoionization, and they complement existing laser–based photoelectron and induced fluorescence methods [12,22–25], confirming technical advantages that have been demonstrated in earlier vibrationally resolved ionization studies [6,28,33].

- With its broad spectral range, the dispersed fluorescence method is suitable for survey studies that can characterize the molecular photoionization dynamics.
- In contrast to the large body study of electron–impact ionization, the fluorescence measurement can be limited by the dipole excitation, so the present result of large ΔN transitions for N_2 shows the non–Boltzmann distribution at high photon energy.

Finally,

4. For the rotationally resolved data,

- The present studies serve to illustrate the effect of Cooper minima, shape resonance, and strong angular momentum mixing in the photoelectron continua on the ion rotational distributions over a broad spectral range well beyond the reach of conventional photoelectron spectroscopy.
- The rotational resolution provides a window on the angular momentum composition of the photoelectron and the partitioning of the angular momentum between the photoelectron and ion core.
- Therefore, this rotationally resolved study is demonstrated to understand fundamental aspects of molecular photoionization.

As future developments to extend this work, some of possibilities are list below.

5. For future developments,

- We need to modify the optical system between the fluorescence monochromator and the detector OMA. Owing to the sensitive dependence of its focal length on wavelengths, the position of the lens has to be moved whenever we are looking for different fluorescence wavelengths. Charge–coupled devices (CCD) which do not require the optical system between the fluorescence monochromator and the detector can eliminate this problem. Also it can function with high quantum efficiency (up to 70 % at 700 nm), high resolution (up to 4096 pixels), and high signal/noise ratio..
- It is possible to probe the photoionization dynamics by selecting the vibrational level of the neutral target molecules. This selection of vibrational level can be accomplished combining a laser system to excite target molecules in the ground electronic state. The rotational level of the target molecules could also then be state–selected. Currently, the target molecules undergoing photoionization are in a thermal distribution of rotational levels. By rotationally selecting the target molecules, complete state–to–state photoionization data could be obtained, providing the similar data from REMPI studies. With the advantage of fluorescence studies for the wide range of the excitation energy, the dynamics of photoionization could be investigated in more detail.
- There are necessary extensions of this work, such as investigating a wide variety of diatomic molecular systems with rotational resolution. The

REMPI technique and single-photon ionization with PES has been employed in studies of several diatomic molecules including NO [12,17,22], O_2 [11], H_2 [10,36], D_2 [8], and other diatomic molecules such as light hydrides, HBr [26] and OH [12]. Previous theoretical and experimental studies have shown clear evidences for the presence of Cooper minima and shape resonances, affecting ion distributions. In many of these cases, the photoelectron detection scheme had insufficient energy resolution for a specific rotational level of the molecular ion and limited excitation energy range. However, highly resolved fluorescence measurements for those samples over a broad spectral range can enrich information for molecular photoionization, illustrating effects such as Cooper minima, shape resonances, and angular momentum mixing in the continuum.

- Polarization measurements following molecular photoionization yields the ratio of dipole strengths for degenerate ionization channels [19]. Since the polarization measurement provides additional information to the angular momentum composition, it is possible to probe another side of molecular photoionization dynamics by determining the magnitudes and phases of dipole transition amplitudes in separate degenerate channels.

REFERENCES

1. J.L.Dehmer, A.C.Parr, and S.H.Southworth, in *Handbook on Synchrotron Radiation, Vol* II, ed. G.V.Marr (North-Holland, Amsterdam, 1987)

2. J.L.Dehmer, D.Dill, and A.C.Parr, in *Photophysics and Photochemistry in the Vacuum Ultraviolet,* ed. S.P.McGlynn, G.L.Findley, and R.H.Huebner (Reidel, Dordrecht, 1985)

3. U.Fano and A.R.P.Rau, in *Atomic Collisions and Spectra* (Academic Press, Orlando, 1986)

4. J.Berkowitz, in *Photoabsorption, Photoionization, and Photoelectron spectroscopy* (Academic Press, New York, 1976)

5. S.Leach in *Photophysics and Photochemistry in the Vacuum Ultraviolet,* ed. S.P.McGlynn, G.L.Findley, and R.H.Huebner (Reidel, Dordrecht, 1985)

6. E.D.Poliakoff, in *Vacuum Ultraviolet Photoionization and Photodissociation of Molecules and Clusters,* edited by C.Y.Ng (World Scientific, Singspore, 1991)

7. S.Kakar, Ph.D. Thesis, Louisiana State University (1993)

8. S.T.Pratt, P.M.Dehmer, and J.L.Dehmer, J. Chem. Phys. **92**,262 (1990); M.A.O'Halloran, P.M.Dehmer, S.T.Pratt, J.L.Dehmer, and F.S.Tomkins, J. Chem. Phys. **90**,930 (1989); W.Peatman, F.P.Wolf, and R.Unwin, Chem. Phys. Lett. **95**,453 (1983)

9. L.Åsbrink, Chem. Phys. Lett. 7,549 (1970)

10. A.Niehaus and M.W.Ruf, Chem. Phys. Lett. **11**,55 (1971); Y.Itikawa, Chem. Phys. **37**,401 (1979); J.E.Pollard, D.J.Trevor, J.E.Reutt, Y.T.Lee, and D.A.Shirley, J. Chem. Phys. 77,34 (1982); D.Dill, Phys. Rev. A**6**,160 (1972)

11. M.Braunstein, V.McKoy, S.N.Dixit, R.G.Tonkyn, and M.G.White, J. Chem. Phys. **93**,5345 (1990); M.Braunstein, S.N.Dixit, and V.McKoy, J. Chem. Phys. **96**,5726 (1992); R.G.Tonkyn, J.W.Winniczek, and M.G.White, Chem. Phys. Lett. **164**,137 (1989)

12. E.de Beer, C.A.de Lange, J.A.Stephens, K.Wang, and V.McKoy, J. Chem. Phys. **95**,714 (1991); K.Wang, J.A.Stephens, V.McKoy, E.de Beer, C.A.de lange, and N.P.C.Westwood, J. Chem. Phys. **97**,211 (1992); K.Wang, J.A.Stephens, and V.McKoy, J. Chem. Phys. **95**,6456 (1991)

13. J.Xie and R.N.Zare, J. Chem. Phys. **93**,3033 (1990)

14. K.Müller–Dethelefs and E.W.Schlag, annu. Rev. Phys. Chem. **42**,109 (1991); K.Müller–Dethelefs, M.Sander, and E.W.Schlag, Chem. Phys. Lett. **112**,291 (1984); M.Sander, L.A.Chewter, K.Müller–Dethelefs, and E.W.Schlag, Phys. Rev. A**36**,4543 (1987)

15. M.-T.Lee, K.Wang, V.McKoy, R.G.Tonkyn, R.T.Wiedmann, E.R.Grant, and M.G.White, J. Chem. Phys. **96**,7848 (1992)

16. K.Wang and V.McKoy, J. Chem. Phys. **95**,4977 (1991)

17. R.T.Wiedmann, M.G.White, K.Wang, and V.McKoy, J. Chem. Phys. **98**,7673 (1993)

18. A.Strobel, I.Fischer, J.Staeker, G.Nieder–Schatteburg, K.Müller–Dethelefs, and V.Bonybey, J.Chem. Phys. **97**,2332 (1992)

19. E.D.Poliakoff, J.L.Dehmer, D.Dill, A.C.Parr, K.H.Jackson, and R.N.Zare, Phys. Rev. Lett. **46**,907 (1981); J.A.Guest, K.H.Jackson, and R.N.Zare, Phys. Rev. A **28**,2217 (1983)

20. R.N.Zare, in *Angular Momentum; Understanding Spatial Aspects in Chemistry and Physics* (John Wiley & Sons, 1988)

21. C.H.Greene and R.N.Zare, Ann. Rev. Phys. Chem. 119 (1982)

22. X.Song, E.Sekreta, J.P.Reilly, H.Rodolph, and V.Mckoy, J. Chem. Phys. **91**,6062 (1989); W.G.Wilson, K.S.Viswanathan, E.Sekreta, and J.P.Reilly, J. Chem. Phys. **88**,672 (1984)

23. K.L.Reid, D.J.Leahy, and R.N.Zare, Phys. Rev. Lett. **68**,3527 (1992)

24. S.T.Pratt, P.M.Dehmer, and J.L.Dehmer, J. Chem. Phys. **78**,4315 (1983)

25. L.F.Dimauro and T.A.Miller, Chem. Phys. Lett. **138**,175 (1987); A.Fujii, T.Ebata and M.Ito, J. Chem. Phys. **88**,5307 (1988); T.Ebata, A.Fujii and M.Ito, J. Phys. Chem **91**,3125 (1987)

26. J.Xie and R.N.Zare, Chem. Phys. Lett. **159**,399 (1989)

27. E.D.Poliakoff, J.C.K.Chan, and M.G.White, J. Chem. Phys. **85**,6232 (1986)

28. S.Kakar, H.C.Choi, and E.D.Poliakoff, J. Chem. Phys. **97**,L6998 (1992)

29. J.D.Bozek, G.M.Bancroft, J.N.Cutler, and K.H.Tan, Phys. Rev. Lett. **65**,2757 (1990); J.D.Bozek, G.M.Bancroft, and K.H.Tan, Phys. Rev. A **43**,3597 (1991)

30. C.T.Chen, Y.Ma, and F.Sette, Phys. Rev. A **40**,6737 (1989)

31. H.C. Choi, R. Rao, A.G. Mihill, S. Kakar, E.D. Poliakoff, K. Wang, and V. McKoy, Phys. Rev. Lett. **72**, 44 (1994)

32. E.D.Poliakoff, M.-H. Ho, G.E.Leroi, and M.G.White, J. Chem. Phys. **84**,4779 (1986)

33. S.Kakar, H.C.Choi, and E.D.Poliakoff, Chem. Phys. Lett. **190**,489 (1992); S.Kakar, H.C.Choi, and E.D.Poliakoff, J. Chem. Phys. **97**,4490 (1992)

34. S.N.Dixit and V.McKoy, Chem. Phys. Lett. **128**,49 (1986); S.N.Dixit and V.McKoy, J. Chem. Phys. **82**,3546 (1985)

35. K.Wang, V.McKoy H.C.Choi, R.Rao, A.G.Mihill, S.Kakar, and E.D.Poliakoff (to be published)

36. S.T.Pratt, P.M.Dehmer, and J.L.Dehmer, Chem. Phys. Lett. **105**,28 (1984); S.T.Pratt, E.F.McCormack, J.L.Dehmer, and P.M.Dehmer, J. Chem. Phys. **92**,1831 (1990)

37. G.Herzberg, in *Molecular Spectra and Molecular Structure*, Vol I Spectra of Diatomic Molecules (Krieger, Malabar, Florida, 1989)

38. E.S.Chang, J. Phys. B**11**,L69 (1978)

39. A.R.Edmonds, in *Angular Momentum in Quantum Mechanics* (Princeton University Press, New Jersey, 1957)

40. J.W.Cooper, Phys. Rev. **128**,681 (1962)

41. S.T.Manson and J.W.Cooper, Phys. Rev. **165**,126 (1968)

42. J.L.Dehmer, D.Dill, Phys. Rev. Lett. **35**,213 (1975); J.L.Dehmer, D.Dill, J. Chem. Phys. **65**,5327 (1976); A.Görling and N.Rösch, J. Chem. Phys. **93**,5563 (1990)

43. M.G.White, G.E.Leroi, M.-H. Ho, and E.D.Poliakoff, J. Chem. Phys. **87**,6553 (1987)

44. K.P.Huber and G.Herzberg, in *Constants of Diatomic Molecules* (Van Nostrand–Reinhold, New York,1979)

45. J.Stõhr, in *NEXAFS Spectroscopy* (Springer–Verlag series in Surface Sciences 25, 1991)

46. L.A.Kelly, L.M.Duffy, B.Space, E.D.Poliakoff, P.Roy, S.H.Southworth, and M.G.White, J. Chem. Phys. **90**,1544 (1989)

47. T.A.Ferrett, A.C.Parr, S.H.Southworth, J.E.Hardis, and J.L.Dehmer, J. Chem. Phys. **90**,1551 (1989)

48. E.P.Muntz, Phys. Fluids, **5**,80 (1962)

49. D.Coe, F.Robben, L.Talbot, and R.Cattolica, Phys. Fluids, **23**,706 (1980); D.Coe, F.Robben, L.Talbot, and R.Cattolica, Phys. Fluids, **23**,715 (1980)

50. R.E.Smalley, L.Wharton, and D.H.Levy, J. Chem. Phys. **11**,4977 (1975)

51. B.C.Craft, M.Feldman, E.Morikawa, E.D.Poliakoff, V.Saile, J.D.Scott, and R.L.Stockbauer, Rev. Sci. Instr. **63**,1561 (1992)

52. E.Morikawa, J.D.Scott, E.D.Poliakoff, R.L.Stockbauer, and V.Saile, Rev. Sci. Instr. **63**,1300 (1992)

53. J.L.Rose, D.C.Mancini, J.T.Welnak, and R.K.Cole, Nuc. Instrum. Meth. A **291**, 192 (1990)

54. J.W.Davenport Phys. Rev. Lett. **36**,945 (1976)

55. F.R.Powell, P.W.Vedder, J.F.Lindblom, and S.F.Powell, Opt. Eng. **29**, 581 (1990)

56. E.W.Plummer, T.Gustafsson, W.Gudat, and D.E.Eastman, Phys. Rev. A **15**,2339 (1977)

VITA

Heung–Cheun Choi was born on Aug. 15, 1956 in Pusan, South Korea. He received the Bachelor of Science degree from Korea University in 1982, and the Master of Science degree from Korea University in 1984. He joined the group of Professor Poliakoff in January 1990.

DOCTORAL EXAMINATION AND DISSERTATION REPORT

Candidate: Heung-Cheun Choi

Major Field: PHYSICS

Title of Dissertation:
ENERGY DEPENDENCE OF PHOTOION ROTATIONAL DISTRIBUTIONS

Approved:

Major Professor and Chairman

Dean of the Graduate School

EXAMINING COMMITTEE:

Date of Examination:

4/6/94